

Universal control of four singlet-triplet qubits

Xin Zhang,^{1,2,*} Elizaveta Morozova,^{1,2,*} Maximilian Rimbach-Russ,^{1,2} Daniel Jirovec,^{1,2} Tzu-Kan Hsiao,^{1,2} Pablo Cova Fariña,^{1,2} Chien-An Wang,^{1,2} Stefan D. Oosterhout,^{1,3} Amir Sammak,^{1,3} Giordano Scappucci,^{1,2} Menno Veldhorst,^{1,2} and Lieven M. K. Vandersypen^{1,2,†}

¹*QuTech, Delft University of Technology, Delft, The Netherlands.*

²*Kavli Institute of Nanoscience, Delft University of Technology, Delft, The Netherlands.*

³*Netherlands Organisation for Applied Scientific Research (TNO), Delft, The Netherlands.*

(Dated: December 29, 2023)

The coherent control of interacting spins in semiconductor quantum dots is of strong interest for quantum information processing as well as for studying quantum magnetism from the bottom up. On paper, individual spin-spin couplings can be independently controlled through gate voltages, but nonlinearities and crosstalk introduce significant complexity that has slowed down progress in past years. Here, we present a 2×4 germanium quantum dot array with full and controllable interactions between nearest-neighbor spins. As a demonstration of the level of control, we define four singlet-triplet qubits in this system and show two-axis single-qubit control of all qubits and SWAP-style two-qubit gates between all neighbouring qubit pairs. Combining these operations, we experimentally implement a circuit designed to generate and distribute entanglement across the array. These results highlight the potential of singlet-triplet qubits as a competing platform for quantum computing and indicate that scaling up the control of quantum dot spins in extended bilinear arrays can be feasible.

The coherent control of a large-scale array of spins in the solid state represents a major challenge in the field of quantum-coherent nanoscience [1–4]. As a quintessential platform for quantum spin control, the lithographically-defined semiconductor quantum dot has shown great promise both for fault-tolerant digital quantum computation [5–15] and for analog quantum simulation of emergent quantum phenomena [16–19]. Nevertheless, the inherent nanoscale dimensions of the devices, the geometrical constraints in integrating all the required components, and the necessity of employing high-frequency electromagnetic fields in cryogenic environments present important challenges for the integration and control a large number of spins.

Already, significant efforts have been undertaken to tackle these challenges. For single-spin qubits, the number of coherently controlled spins has been scaled up to six in a one-dimensional array [11] and four in a two-dimensional array [10]. A six-dot linear array was also used to achieve universal control of two qubits that are each encoded in a subspace of three electron spins distributed over three dots [15]. For singlet-triplet qubits defined in a subspace of two spins across two dots, recent progress includes the individual control of three to four uncoupled qubits [20, 21] and the operation of a single qubit in a 3×3 quantum dot array [22].

Similar to exchange-only qubits, singlet-triplet qubits [6, 13, 14, 21, 23–30] allow fully electrical qubit control using baseband voltage pulses. The use of baseband-only control signals can avoid commonly encountered problems of single-spin qubits such as microwave heating effects [11, 31, 32] and may furthermore

alleviate crosstalk effects [33]. Singlet-triplet qubits also map naturally to the spin-readout basis in Pauli spin blockade (PSB), which is a common method for spin-to-charge conversion in quantum dots [24, 34]. By using pulse optimization, single-qubit control fidelities of singlet-triplet qubits have exceeded 99% [28], whereas two-qubit gate fidelities relying on the relatively weak capacitive (Coulomb) interaction reached 72–90% [13, 14]. In theory, the two-qubit gate fidelity can be further improved by replacing the capacitive coupling with the stronger exchange coupling [29], although it has been little investigated in experiments [35]. Despite this progress, universal control of more than two interacting singlet-triplet qubits remains yet to be achieved. Recently, a controlled number of charge carriers were loaded in 2×4 arrays, a 4×4 array and a 1×12 array [36–40]. These advances set the stage for exploring the operation of three or more interacting singlet-triplet qubits experimentally.

Here we demonstrate coherent control of four interacting singlet-triplet qubits in a 2×4 germanium quantum dot array, which forms a quantum dot ladder. Taking advantage of the strong intrinsic spin-orbit coupling and small in-plane g-factors of holes in strained germanium quantum wells [41], we encode the qubit in the singlet ($|S\rangle$) and the lowest triplet ($|T_-\rangle$) of two exchange-coupled spins, a variant of the originally proposed singlet-triplet qubit [19, 42–49]. By controlling the exchange interaction inside each spin pair along the ladder rungs, we first map out the qubit energy spectrum. Then we show universal control of each qubit by pulsing both the detuning and tunneling barrier of the corresponding double quantum dot (DQD). With proper simultaneous control of detunings and tunneling barriers of neighbouring $S - T_-$ qubits, we achieve a two-qubit SWAP-style gate induced by exchange interactions for each pair of neigh-

* These authors contributed equally to this work

† L.M.K.Vandersypen@tudelft.nl

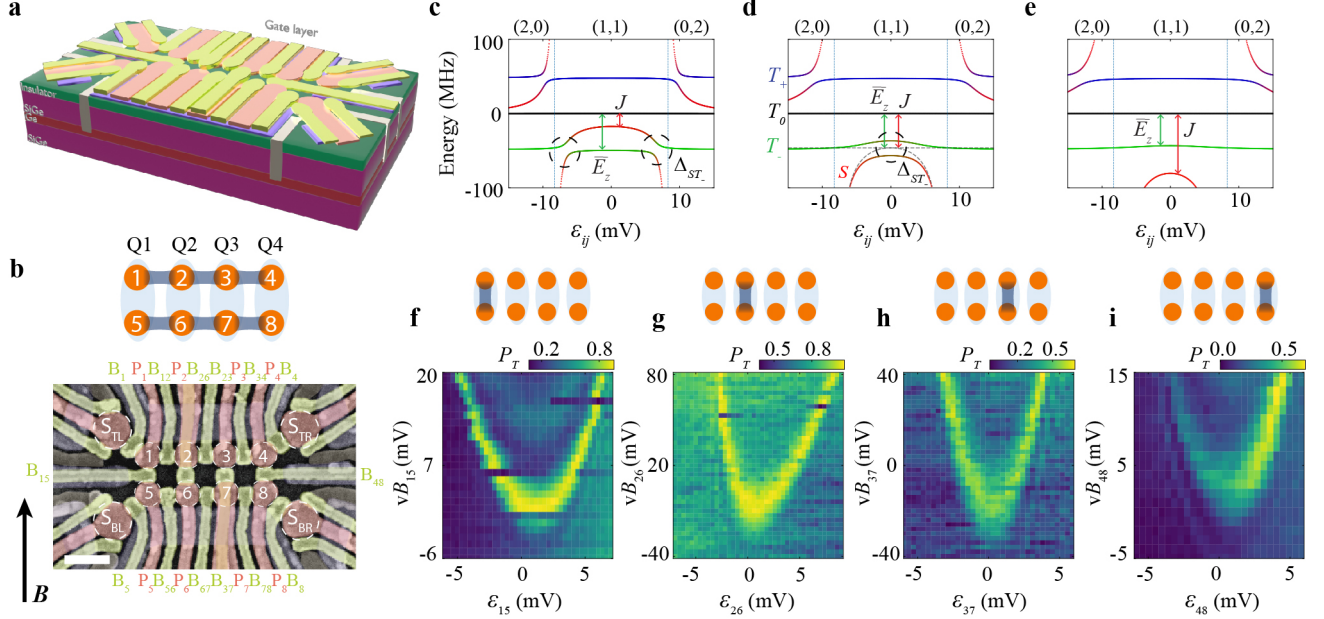


FIG. 1. **Device and energy spectroscopy.** **a**, Schematic drawing showing the Ge/SiGe heterostructure and three layers of gate electrodes on top to define the quantum dot ladder and sensing dots: screening gates (purple), plunger gates (red), barrier gates (green). Ohmic contacts (light green) extend towards the Ge quantum well in which the holes are confined. The aluminum oxide dielectric between different gate layers is omitted for clarity. **b**, False-colored scanning electron microscope image of a device nominally identical to that used in the measurements, where the in-plane position of the 8 quantum dots is indicated with numbers 1-8 in circles. Charge sensors close to the ladder corners are labeled within larger circles. The plunger (red) and barrier (green) gates of the quantum dots are labeled outside the image. A schematic of the ladder structure of the quantum dots is shown on top, with Q1-Q4 formed by vertical double quantum dots (DQD). **c-e**, The energy levels of two-spin states in a DQD as a function of energy detuning ε_{ij} between dot i and j with from left to right the case $J(\varepsilon_{ij} = 0) < \bar{E}_z$, $J(\varepsilon_{ij} = 0) = \bar{E}_z$, $J(\varepsilon_{ij} = 0) > \bar{E}_z$. The dashed black circles denote the positions of $S - T_-$ anticrossings. **f-i**, The measured energy spectra that probe the positions of the $S - T_-$ anticrossings as a function of the detuning and the barrier gate voltage for each vertical DQD. The color scale shows the measured spin triplet probability P_T after initializing a vertical DQD in a singlet state (in (0,2) or (2,0)) and applying a gate voltage pulse (20 ns ramp in, 40 ns wait time, 0 ns ramp out) to the detuning shown on the horizontal axis, for different vB_{ij} .

bouring qubits in the ladder. Finally, with the demonstrated single- and two-qubit control, we implement a quantum circuit for quantum state transfer across the ladder.

I. GERMANIUM QUANTUM DOT LADDER

As shown in Fig. 1a and b, the 2x4 quantum dot ladder is fabricated in a germanium quantum-well heterostructure [50]. The gate pattern and substrate have the same design as that in ref. [38]. The eight quantum dots are labeled with numbers 1 to 8 and the four charge sensors to measure the charge states in the quantum dots are labeled S_{TL} , S_{TR} , S_{BL} and S_{BR} , respectively. The quantum dot potentials are controlled by plunger gates P_i , and the interdot or dot-sensor tunnel couplings are controlled by barrier gates B_{ij} or B_i , with i or j denoting the corresponding quantum dot number. Linear combinations of plunger gate voltages $\{P_i\}$ allow us to set the overall elec-

trochemical potential of each DQD $\mu_{ij} = (vP_i + vP_j)/2$ and the interdot detuning $\varepsilon_{ij} = (vP_i - vP_j)/2$. The prefix “v” indicates that the physical gate voltages are virtualized to compensate the crosstalk on the dot potentials [16] (see Supplementary Information section III for the virtual gate matrix). Single-hole occupation of each quantum dot in the array is confirmed by measuring the charge stability diagrams using sensors S_{BL} and S_{BR} (see Supplementary Information section II). All plunger and interdot barrier gates are connected to a bias tee to allow both DC voltages and voltage pulses to be applied.

II. SINGLET-TRIPLET QUBIT AND ENERGY SPECTROSCOPY

We encode the qubit into the two-spin singlet-triplet states, $|S\rangle$ and $|T_-\rangle$, of the DQDs along the rungs of the quantum dot ladder, with the singlet $|S\rangle = (|\uparrow\downarrow\rangle - |\downarrow\uparrow\rangle)/\sqrt{2}$ and the lowest-energy triplet $|T_-\rangle = |\downarrow\downarrow\rangle$. Thus

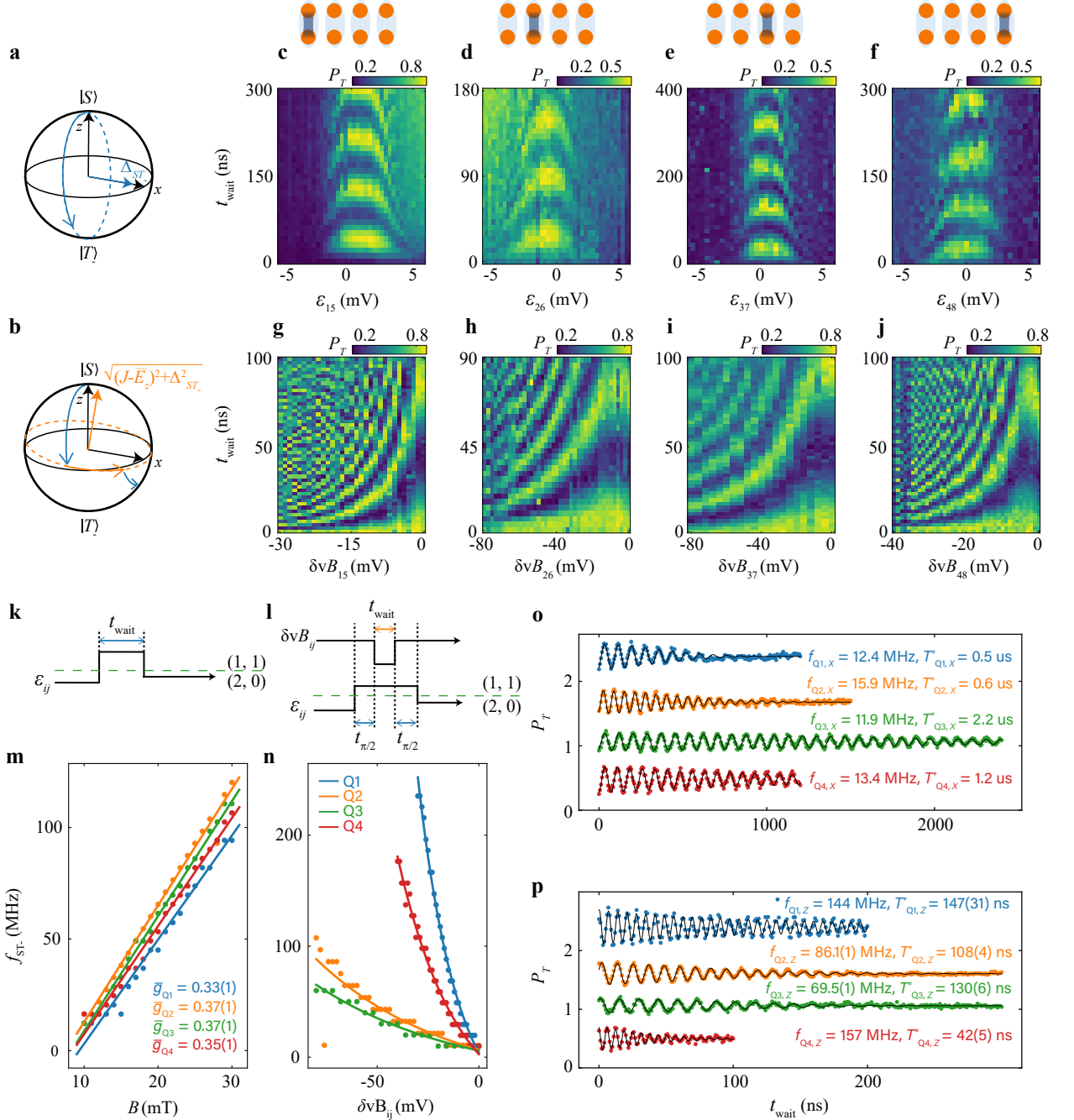


FIG. 2. Universal single-qubit control of four singlet-triplet qubits. **a,b**, Illustration of x -axis and z -axis evolution of $S - T_-$ qubits in the Bloch sphere. The straight blue and orange arrows show the corresponding rotation axis. The x -axis rotations are set by the $S - T_-$ coupling, Δ_{ST_-} . For large J such that $J - \bar{E}_z \gg \Delta_{ST_-}$, the rotation axis tilts towards the z -axis. **c-f**, Experimental results for x -axis rotations of each qubit, showing measured triplet probabilities P_T as a function of t_{wait} and the detuning voltage ε_{ij} . **g-j**, Experimental results for z -axis rotations of each qubit, showing P_T as a function of t_{wait} and the barrier voltage change $\delta v B_{ij}$. **k,l**, The pulse schemes used for x -axis control (**k**) and z -axis control (**l**). In experiments, the detuning pulse in **k** and **l** has a 20 ns ramp (not shown) from $(2, 0)$ to $(1, 1)$ to ensure adiabaticity with respect to the $S-T_0$ splitting. **m**, The rotation frequency f_{ST_-} of each qubit as a function of the magnetic field strength B . The data are acquired using the fast Fourier transform (FFT) of time-domain oscillations (initiated using a ramp time of 100 ns, see Supplementary Information section V for more details and for the time-domain data of **m**). **n**, The rotation frequency f_{ST_-} of each qubit as a function of $\delta v B_{ij}$, extracted from panels **g-j** using FFT. The data points for Q2 and Q3 show some steps as the barrier gate voltage is changed, which are limited by the FFT precision. The solid lines are fits of the data with an exponential function. **o-p**, The measured triplet probabilities P_T of long-time evolutions around the x - (**o**) and z -axis (**p**) for Q1-Q4. The data is vertically shifted for clarity. In **o**, the detuning is around 0 mV. In **p**, we take the data with the same detuning but with different barrier voltage pulses: $\delta v B_{15} = -20$ mV, $\delta v B_{26} = -80$ mV, $\delta v B_{37} = -80$ mV, and $\delta v B_{48} = -30$ mV. The barrier voltages are chosen to achieve the condition $J - \bar{E}_z \gg \Delta_{ST_-}$ depending on the gate tunability. For more measurement details, see Supplementary Information section II.

Q1, Q2, Q3 and Q4 are formed using DQD 1-5, 2-6, 3-7 and 4-8. Qubit readout is achieved by pulsing the corresponding DQD to the PSB regime. This regime converts the singlet and triplet states into distinct charge states, which are then measured through the charge sensor. The single-qubit Hamiltonian can be written as

$$H_{ST_-} = \frac{\bar{E}_z - J}{2} \sigma_z + \frac{\Delta_{ST_-}}{2} \sigma_x, \quad (1)$$

where σ_x and σ_z are the Pauli matrices, $J = J(\varepsilon_{ij}, vB_{ij})$ is a function of both the detuning ε_{ij} and the barrier gate voltage vB_{ij} , and $\bar{E}_z = \bar{g}_{ij} \mu_B B$ is the average Zeeman energy of the two hole spins in the DQD, with \bar{g}_{ij} the average g -factor, μ_B the Bohr magneton, and B the magnetic field strength. Unless indicated otherwise, an in-plane magnetic field (up to alignment precision) of $B = 10$ mT is applied to the device. The intrinsic spin-orbit interaction for holes in germanium couples the states $|S\rangle$ and $|T_-\rangle$ with an energy Δ_{ST_-} .

Figs. 1c-e show the energy levels of the two-spin $|S\rangle$ and $|T_-\rangle$ states in a DQD with $J(\varepsilon_{ij} = 0) < \bar{E}_z$, $J(\varepsilon_{ij} = 0) = \bar{E}_z$, $J(\varepsilon_{ij} = 0) > \bar{E}_z$, respectively. The other two-spin states are $|T_0\rangle = (|\uparrow\downarrow\rangle + |\downarrow\uparrow\rangle)/\sqrt{2}$ and $|T_+\rangle = |\uparrow\uparrow\rangle$. In a DQD, we can describe the charge states as (n_L, n_R) to denote the charge number distribution in the left (n_L) and right (n_R) quantum dot. By adjusting the detuning ε_{ij} of the DQD from negative to positive, we can change the charge state from (2,0) to (1,1) and then to (0,2), as indicated by the labels on top of each diagram, and the energy levels of the two-spin states in the DQD will change accordingly. As shown in Fig. 1c, when $J(\varepsilon_{ij} = 0)$ is smaller than \bar{E}_z , the singlet $|S\rangle$ crosses the triplet $|T_-\rangle$ twice in the (1,1) regime. Due to intrinsic spin-orbit coupling, these are in fact avoided crossings with a gap Δ_{ST_-} , where the states $|S\rangle$ and $|T_-\rangle$ are admixed. As $J(\varepsilon_{ij} = 0)$ increases, the two anticrossings approach each other and eventually merge into one, as shown in Fig. 1d. When $J(\varepsilon_{ij} = 0)$ increases even further, see Fig. 1e, $|S\rangle$ and $|T_-\rangle$ no longer exhibit an avoided crossing.

Experimentally, we probe the position of the avoided crossings as follows. First, we initialize one of the qubits to a singlet by diabatically pulsing from (0,2) or (2,0) to the detuning ε_{ij} in (1,1). After waiting for a certain time, we pulse the qubit back to the PSB regime to record the triplet probability. When the pulse takes the system to an anticrossing, the singlet will evolve into a triplet during the waiting time (a 40 ns duration is chosen to obtain a sizable triplet probability). Performing such measurements as a function of the barrier gate voltage vB_{ij} that controls J for each qubit, results in the parabolic-like patterns, also called spin mixing maps [22, 51], in Fig. 1f-i. As expected, when vB_{ij} is tuned from positive to negative, J increases and the positions of the $S - T_-$ anticrossings move inwards before disappearing. The asymmetry visible in panel g in particular can arise from imperfect virtualization of the barrier gates or from a detuning-dependent Zeeman energy [52] (see Supplementary Information section IV).

III. UNIVERSAL SINGLE-QUBIT CONTROL

With the knowledge of the energy spectrum of the four $S - T_-$ qubits, we next implement the two-axis control of each qubit, which is necessary and sufficient for universal single-qubit control. By operating the qubit in the regime where $J = \bar{E}_z$, the first term of Eq. 1 goes to zero and Δ_{ST_-} rotates the qubit around the x -axis in the Bloch sphere, as shown in Fig. 2a. Furthermore, we tune the barrier voltage to obtain $J = \bar{E}_z$ at zero detuning, which is a symmetry point where the effect of detuning noise is strongly suppressed [53, 54]. The pulse scheme for testing x -axis control is shown in Fig. 2k: first we initialize the qubit into a singlet by starting in the (2,0) (or (0,2)) regime, then pulse the detuning to the center of the (1,1) regime where $J(\varepsilon_{ij} = 0) = \bar{E}_z$, next allow the qubit to evolve for a variable time t_{wait} , and finally pulse the detuning back to a point in the (2,0) (or (0,2)) regime for spin readout via PSB. The measured rotations of Q1-Q4 as a function of the pulsed detuning position are shown in Fig. 2c-f. With proper calibration, the qubits rotate around the x -axis at zero detuning (this condition occurs slightly away from the point $\varepsilon_{ij} = 0$ extracted from charge stability diagrams).

To realize z -axis control, we operate the Hamiltonian in the opposite limit where we increase J to such a large value that the effect of spin-orbit coupling becomes negligible. As a result, the qubit is rotated around an axis close to the z -axis, with a frequency proportional to $J - \bar{E}_z$. The rotation is never exactly around the z -axis due to the presence of a finite Δ_{ST_-} , yet, sufficiently orthogonal control is possible when $(J - \bar{E}_z) \gg \Delta_{ST_-}$ (furthermore, by finely tuning the magnet field direction, $\Delta_{ST_-} = 0$ can be achievable [46, 49]). In experiments, we perform a Ramsey-like pulse sequence to demonstrate z -axis control. As illustrated in Fig. 2b and l, we first initialize the qubit into a singlet, perform a $\pi/2$ rotation around the x -axis of duration $t_{\pi/2}$, and then change J diabatically by pulsing the corresponding barrier gate by an amount δvB_{ij} to implement a z -axis rotation. Throughout the barrier gate pulse, we aim to stay at the symmetry point to minimize the sensitivity to charge noise [53, 54]. Finally, we perform another $\pi/2$ operation around the x -axis and project the qubit into the $S - T_-$ basis for spin readout.

The measured z -axis rotations as a function of the change of barrier voltage δvB_{ij} for the four qubits are shown in Fig. 2g-j. The oscillation frequency is given by $f_{ST_-} = \sqrt{(J - \bar{E}_z)^2 + \Delta_{ST_-}^2}/h$, where h is Planck's constant. Fig. 2n summarizes how f_{ST_-} can be tuned via δvB_{ij} . We note that the outer two barrier gates vB_{15} and vB_{48} have a stronger effect on the corresponding J_{ij} than the inner barrier gates vB_{26} and vB_{37} . This may be explained by additional residues below the inner barrier gates, which are fabricated in the last step [38], and by the different fan-out routing for the outer barrier gates (see Fig. 1a,b). With the tuning range shown in panel n,

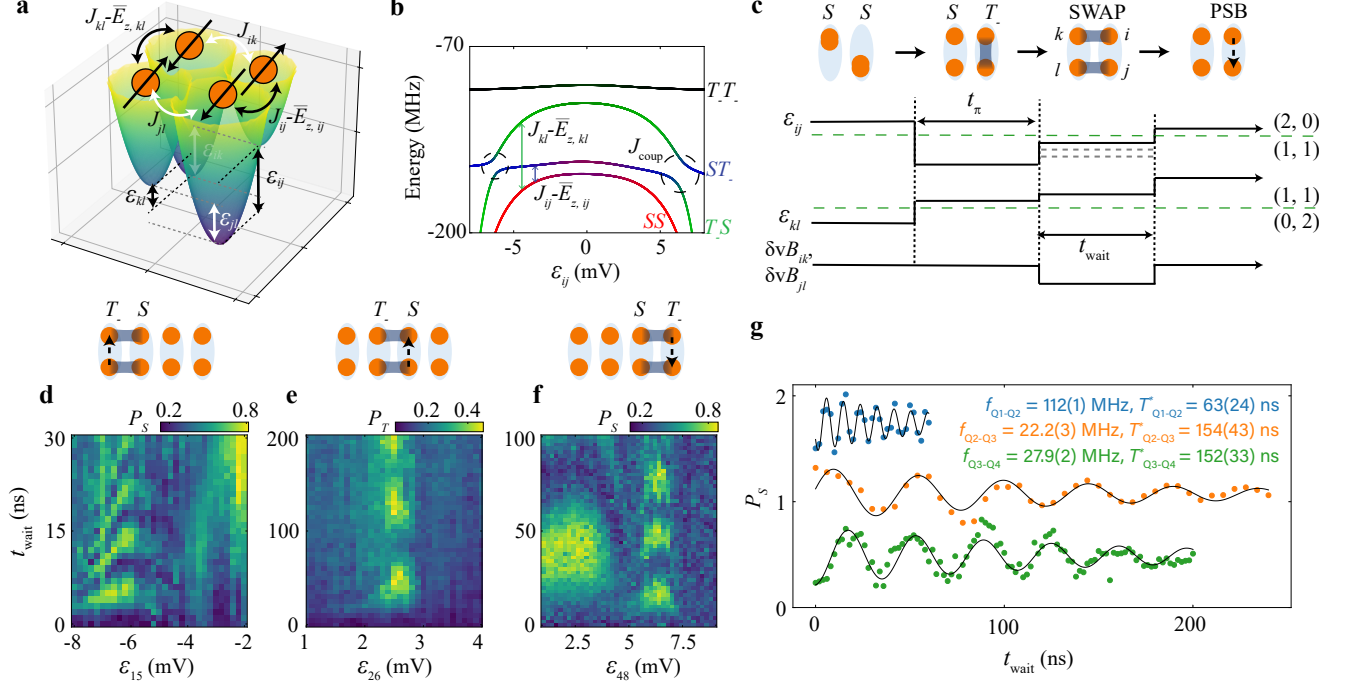


FIG. 3. Two-qubit interactions across the quantum dot ladder. **a**, A plaquette of two connected DQDs. The $S - T_-$ qubits have a splitting of $J_{ij} - \bar{E}_{z,ij}$ and $J_{kl} - \bar{E}_{z,kl}$ (neglecting Δ_{ST_-}), which are controlled by the detunings ε_{ij} and ε_{kl} , respectively. The qubit-qubit coupling J_{coup} is an average of J_{ik} and J_{jl} between the corresponding dots, which are controlled by ε_{ik} and ε_{jl} . **b**, The energy levels of two-qubit states, where we fix ε_{kl} to be positively large and scan ε_{ij} . At the positions where $J_{ij} - \bar{E}_{z,ij}$ equals $J_{kl} - \bar{E}_{z,kl}$, an anticrossing with a gap J_{coup} forms (black dashed circles), which can be used to induce SWAP oscillations between $|ST_- \rangle$ and $|T_-S \rangle$. The parameters we use in this calculation are based on the experimental results for Q3-Q4 shown in panel **f**. **c**, The pulse scheme for SWAP operations. We start in $(0,2)$ or $(2,0)$, at large positive or negative detuning, and diabatically pulse one qubit to $(1,1)$ at modest detuning such that it remains in $|S \rangle$, and pulse the other qubit to zero detuning where a π rotation for a time t_π takes it to $|T_- \rangle$. At this point, the qubits are set to $|ST_- \rangle$ or $|T_-S \rangle$. Next, we pulse the detunings of both qubits to make their energies resonant, while at the same time activating J_{ik} and J_{jl} . This will kickstart SWAP oscillations between the two qubits. The dashed lines in the pulse of ε_{ij} show that we scan the detuning of one qubit to find the condition for SWAP operations. After an evolution time t_{wait} , we pulse the detunings to the PSB readout configuration for one of the qubits. **d-f**, The experimental results of SWAP oscillations, showing measured singlet probabilities P_S or triplet probabilities P_T as a function of operation time t_{wait} and the detuning voltage for Q1-Q2 (**d**), Q2-Q3 (**e**) and Q3-Q4 (**f**). The initial states of two qubits (before the SWAP oscillations) are denoted on the top, and the qubit pair that is read out is indicated by the dashed arrow showing the readout pulse direction. **g**, Measured singlet probabilities P_S as a function of the evolution time t_{wait} at the center of the chevron patterns of the SWAP oscillations for each pair of qubits, with a detuning voltage $\varepsilon_{15} = -6$ mV, $\varepsilon_{26} = 2.2$ mV, and $\varepsilon_{48} = 6.2$ mV. The conditions are slightly different from the data in **d-f** due to device tuning.

the highest ratio $(J - \bar{E}_z)/\Delta_{ST_-}$ amounts to around 20 for the outer qubits Q1 and Q4 and about 10 for the inner qubits Q2 and Q3. When the external magnetic field strength is varied while keeping the gate voltages fixed, the oscillation speed increases linearly with the field due to the contribution from Zeeman energy in f_{ST_-} (see Fig. 2m). From the slope, we extract \bar{g}_{ij} for the four qubits, obtaining values of 0.33(1) - 0.37(1), similar to previous devices [10].

The dephasing time under free evolution, which is traditionally termed T_2^* , is an important metric for assessing the qubit quality. Since the qubit rotations around both the x -axis and the z -axis are the result of free evolution, we here introduce T_x^* and T_z^* to describe

the corresponding dephasing times. Fig. 2o,p show the measured damped oscillations of the qubits under x -axis and z -axis control, to which we fit with a function $P_T = P_0 + A \cos(2\pi f t + \phi) \exp[-(t/T^*)^\beta]$. P_0 , A , β , f , T^* are fitting parameters, where f refers to the oscillation frequency and T^* refers to T_x^* or T_z^* . From the fits, we obtain a T_x^* of 0.5 - 2.1 μs and a T_z^* of 42(5) - 147(31) ns. The measured values of T_x^* are slightly lower than previously reported values measured at $B = 3$ mT [19] under the same condition that B is parallel to the hole movement direction. This can be partly attributed to the larger magnetic field in the present experiment: Δ_{ST_-} scales with B [44, 45] and not only sets f_{ST_-} but also constitutes a proportionality factor between noise and

f_{ST_-} fluctuations (see also Supplementary Information section VIII). The extracted x -axis rotation frequencies in Fig. 2o reflect the values of Δ_{ST_-} for each qubit, which are around 11.9-15.9 MHz, nearly an order of magnitude larger than the results reported at $B = 3$ mT [19]. This confirms that Δ_{ST_-} is stronger in the present experiment than in the previous work at 3 mT. The small variation in Δ_{ST_-} and in the measured average g -factors suggests a homogeneous spin-orbit coupling in this device. In comparison, the variations in T_x^* are quite large, which may be caused by spatially dependent charge noise or inhomogeneous hyperfine-induced dephasing due to dot size differences [55].

We also observe that T_z^* is nearly an order of magnitude smaller than T_x^* . Possibly this is due to the fact that fluctuations in the tunnel barrier translate to fluctuations in J , which couple in directly during z -axis evolution but only to second order for x -axis evolution [56, 57]. Additionally, the increased curvature of the singlet branch for larger J implies a higher sensitivity to detuning noise. The variations in J thus may contribute to the spread of the T_z^* values we obtained in Fig. 2p.

IV. TWO-QUBIT GATE

In order to realize universal control of the full four-qubit register, we need to complement single-qubit gates with two-qubit entangling gates. Assuming isotropic exchange interactions between adjacent $S - T_-$ qubits, the two-qubit Hamiltonian in the basis of $\{|SS\rangle, |ST_-\rangle, |T_-S\rangle$ and $|T_-T_-\rangle\}$ can be written as:

$$\begin{aligned}
 H_{2Q} = & \frac{(\overline{E}_{z,ij} - J_{ij})\sigma_z^{ij} + \Delta_{ST_-,ij}\sigma_x^{ij}}{2} + \\
 & \frac{(\overline{E}_{z,kl} - J_{kl})\sigma_z^{kl} + \Delta_{ST_-,kl}\sigma_x^{kl}}{2} + \\
 & \frac{J_{\text{coup}}}{4} [\sigma_x^{ij}\sigma_x^{kl} + \sigma_y^{ij}\sigma_y^{kl} + \frac{1}{2}(\sigma_z^{ij} - I)(\sigma_z^{kl} - I)],
 \end{aligned} \tag{2}$$

where ij and kl refer to the respective qubit dot pair, and the interqubit coupling $J_{\text{coup}} = (J_{ik} + J_{jl})/2$. The coupling term is reminiscent of two well-known interaction Hamiltonians. If the factor $1/2$ of the $\sigma_z\sigma_z$ coupling term were 1 instead, we recover the exchange Hamiltonian that generates the SWAP gate and the universal $\sqrt{\text{SWAP}}$ gate. If that factor were zero, only the flip-flop terms would survive, which generate the $i\text{SWAP}$ and $\sqrt{i\text{SWAP}}$ gate. The coupling Hamiltonian in Eq. 2 thus generates a SWAP-style gate that is not a standard two-qubit gate but is also universal from the perspective of quantum computing (see Supplementary Information section VIII). For simplicity, we call it a SWAP gate in the remainder of this work.

To activate the SWAP gate, we equalize the energy splittings of two qubits and turn on J_{ik} and J_{jl} such that the flip-flop terms can exchange the qubit populations (note that if the qubit energies were set very different

from each other, a CZ gate would result instead). Our strategy for meeting both requirements at the same time is to use the interdot detuning of both qubits [18, 19]. A typical potential landscape for the two qubits in DQD ij and kl is shown in Fig. 3a, where we pulse ε_{ij} to large positive and ε_{kl} to large negative detuning. The detunings ε_{ik} and ε_{jl} , which control the interactions between the qubits, are then automatically increased as well. Therefore, all the exchange interactions involved are enhanced simultaneously and the effect of the single-qubit terms σ_x is made negligible. In practice, we fix the (large) detuning of one qubit and fine-tune that of the other to find the position where two qubits have equal energy splittings. This is illustrated by the energy spectrum in Fig. 3b, where we fix the detuning ε_{kl} to a large negative value and scan the detuning ε_{ij} . We see that the states $|ST_-\rangle$ and $|T_-S\rangle$ anticross at the two positions where $J_{ij} - \overline{E}_{z,ij}$ is equal to $J_{kl} - \overline{E}_{z,kl}$. The gap size is given by J_{coup} . Since ε_{ik} and ε_{jl} , which control J_{coup} via J_{ik} and J_{jl} , are also dependent on ε_{ij} , the sizes of the two gaps are not necessarily the same.

Fig. 3c shows an example of the pulse scheme we use in the experiment to observe two-qubit SWAP oscillations. Starting from both qubits in $(0,2)$ or $(2,0)$, we initialize one qubit to $|T_-\rangle$ using single-qubit control by pulsing ε_{ij} to zero and waiting for a π rotation, and we initialize the other qubit to $|S\rangle$ by pulsing ε_{kl} to a large value in $(1,1)$ (other qubits are either initialized to singlets by pulsing back and forth to $(0,2)$ or $(2,0)$, or remain in the $(1,1)$ regime all the time). Then we pulse the detuning of one qubit such that the energies of the two qubits match, and SWAP oscillations are initiated. Simultaneously, several barrier voltages are pulsed to help set the respective exchange-interaction strengths to appropriate values (details of these pulses vary).

Fig. 3d-f show the resulting SWAP oscillations for Q1-Q2, Q2-Q3, and Q3-Q4. Chevron-style patterns are observed with the energies of the two qubits aligned in the middle of the patterns. Moving away from the middle, the energy of one qubit is shifted with respect to that of the other. This qubit-qubit energy detuning tilts the rotation axis and accelerates the rotation. Looking closely, the chevron patterns are not symmetrical. This can be understood by the fact that the qubit energy does not vary linearly with detuning. In some panels, single-qubit oscillations around an axis close to the x -axis are also observed, such as the data at $\varepsilon_{15} = -2$ mV in Fig. 3d and that at $\varepsilon_{48} = 2.5$ mV in Fig. 3f. These ε_{ij} values are close to zero interdot detuning, and when $J(\varepsilon_{ij} = 0)$ is not much larger than \overline{E}_z , such rotations are expected. We note that SWAP oscillations between $|ST_-\rangle$ and $|T_-S\rangle$ were also observed in previous research on simulating the dynamics of an antiferromagnetic spin chain and resonating-valence-bond states based on the Heisenberg model in four-quantum-dot systems [18, 19].

The oscillation frequencies in the middle of the chevron patterns are in the range of 22.2(3) - 112(1) MHz, corresponding to a $\sqrt{\text{SWAP}}$ (entangling) gate with dura-

tions of just 2.2 ns to 11.3 ns, more than an order of magnitude faster than the entangling gate based on capacitive coupling [13, 14]. To determine the dephasing times of the SWAP oscillations, we collect data in the middle of the chevron patterns, as shown in Fig. 3g, and fit them with the same function as used for single-qubit oscillations. The extracted dephasing times are between 63(24) and 154(43) ns. The dephasing times may be further increased by executing the SWAP oscillations at the symmetry points of the detuning of each qubit, which requires a stronger tunability of the exchange interactions using the barrier gates.

V. QUANTUM CIRCUIT IMPLEMENTATION

Finally, using a combination of the single- and two-qubit gates demonstrated above, we aim to implement a quantum circuit designed to create and distribute an entangled state. As shown in Fig. 4a, we first initialize Q1 and Q2 into $|ST_-\rangle$ by applying a π rotation on Q2 and then activate a SWAP interaction between Q1 and Q2 for a duration t_{SWAP} . This interaction is expected to generate entanglement when t_{SWAP} corresponds to a quarter period, i.e. for a $\sqrt{\text{SWAP}}$ gate. Next, we apply consecutive half-period SWAP gates of Q2-Q3 and Q3-Q4 to transfer the state of Q2 to Q4 via Q3. Finally, we perform a single-qubit x -axis rotation of Q4 for a time t_{Q4} and measure Q4.

The experimental results are shown in Fig. 4b, where the single-qubit oscillations of Q4 as a function of t_{Q4} are modulated in phase by t_{SWAP} , resulting in a checkerboard pattern. The underlying mechanism is that the state of Q2 oscillates as a function of t_{SWAP} , as quantum information is periodically exchanged between Q1 and Q2. Therefore the state of Q4 following the quantum state transfer also oscillates with t_{SWAP} . Where the evolution of Q4 changes phase, t_{SWAP} corresponds to the duration of a $\sqrt{\text{SWAP}}$ operation (modulo an integer number of SWAP operations), at which point maximal entanglement between Q1 and Q2 is expected. When two qubits are maximally entangled, the density matrix of each qubit by itself is fully mixed. At this point, the measured P_T of Q4 should not oscillate as a function of t_{Q4} . This is indeed what we observe, see Fig. 4d, where we show the linecuts from Fig. 4b. A trace without oscillations is observed between two sets of out-of-phase oscillations of Q4, as expected. The same features are seen in Fig. 4c, which shows the ideally expected checkerboard pattern obtained from numerical simulations of the protocol of Fig. 4a, assuming perfect initialization, operations and readout.

We note the checkerboard pattern is quite robust to errors in the SWAP gates. Small errors will merely change the contrast of the pattern; for large SWAP errors, the alternating rows are no longer equal in height. However, when the initialization of Q1 or Q2 leads to superposition states with a y -axis component (and assuming perfect

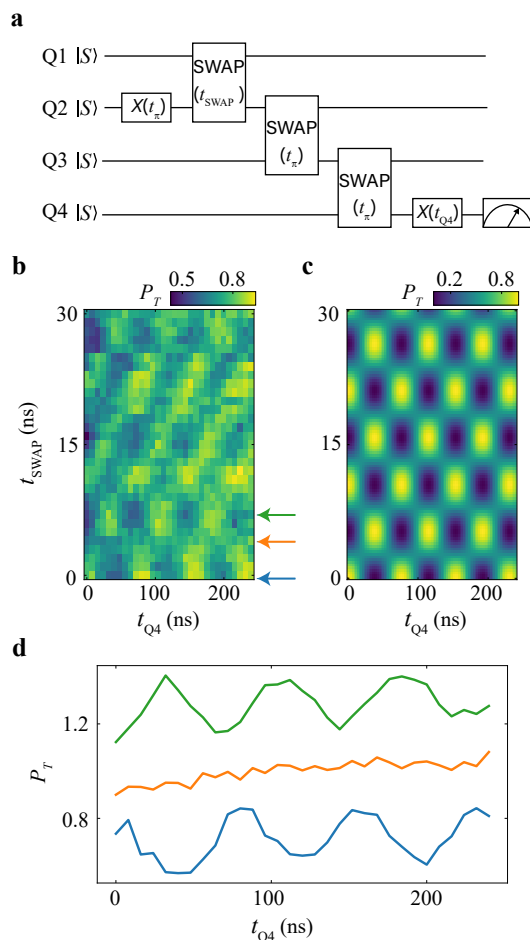


FIG. 4. **Implementation of a quantum circuit for entanglement generation and quantum state transfer.** **a**, Quantum circuit with all the qubits initialized into the singlet. A π rotation around the x -axis (32 ns) rotates Q2 into a triplet state, and a SWAP interaction for a variable time t_{SWAP} periodically produces entanglement between Q1 and Q2. Two subsequent SWAP gates (30 ns and 24 ns) transfer the state of Q2 to Q4 and a final single-qubit rotation of Q4 for a variable time t_{Q4} is followed by the Q4 readout. The delay time between each quantum gate is set to zero. **b,c**, Experimental (**b**) and numerical (**c**) results after running the quantum circuit of panel **a**, with triplet probabilities P_T of Q4 shown as a function of t_{SWAP} and t_{Q4} . **d**, Linecuts from **a** showing triplet probabilities P_T of Q4 as a function of control time t_{Q4} . The data is vertically shifted for clarity.

SWAP gates), the pattern acquires a tilt. In this case, the rotation angle of the final x -axis rotation needed to maximize or minimize P_T is no longer exactly 0 or π but depends on the y -axis component of Q4 (and hence also on t_{SWAP}) after the sequence of SWAP operations. Looking closely, the blue and green oscillations in Fig. 4d are not perfectly out of phase with each other, and the data in Fig. 4b shows weak diagonal features not seen in the numerical simulations. These point at the imperfect initialization of Q1 or Q2.

VI. CONCLUSION

In conclusion, we have experimentally demonstrated initialization, readout, and universal control of four singlet-triplet ($S - T_-$) qubits in a 2x4 germanium quantum dot array. The intrinsic spin-orbit coupling in germanium combined with tunnel barrier control of the exchange interactions within each qubit, allows us to realize two-axis control of the four individual $S - T_-$ qubits using baseband signals only. Furthermore, through independent control of the exchange interactions between any pair of neighbouring spins across the device, we are able to demonstrate $\sqrt{\text{SWAP}}$ and SWAP gates for each neighboring pair of qubits and implement a quantum circuit that spans the entire array. With four universally controlled qubits in a bilinear array, these results put baseband-controlled singlet-triplet spin qubits in germanium firmly on the map as a potential candidate for large-scale quantum computing.

In future experiments, the control fidelities and error channels of these qubits can be thoroughly characterized by various metrology methods such as randomized benchmarking and gate set tomography [7, 15]. The qubit quality and control fidelity can be potentially improved by tuning the qubits into the operational sweet spot with respect to the electric field or magnetic field [55, 58, 59], optimizing control pulses [28, 47], reducing charge noise [60], further improvements in the Ge/SiGe heterostructure [61, 62], and suppressing nuclear spin noise using substrates with reduced spinful nuclei [41]. Moreover, with programmable control of exchange interactions in the array, this spin ladder can also be used for analog simulation of a wealth of rich physical

phenomena such as quantum magnetism [63].

ACKNOWLEDGMENTS

We thank C. Déprez for insightful discussions and kind help. We also thank other members of the Vandersypen group and Veldhorst group for their stimulating discussions. We acknowledge S. L. de Snoo's help in software development and technical support by O. Benningshof, J. D. Mensingh, R. Schouten, R. Vermeulen, R. Birnholtz, E. Van der Wiel, and N. P. Alberts. This work was funded by an Advanced Grant from the European Research Council (ERC) under the European Union's Horizon 2020 research. M.R.-R. acknowledges support from the Netherlands Organization of Scientific Research (NWO) under Veni grant VI.Veni.212.223.

Author contributions X.Z. and E.M. performed the experiment and analyzed the data with help from M.R.-R. and D.J.. X.Z. performed the numerical simulations with help from M.R.-R. and D.J.. M.R.-R. developed the theory model. T.-K.H., P.C.F. and C.-A.W. contributed to the preparation of the experiments. S.D.O. fabricated the device with inputs from T.-K.H., P.C.F. and X.Z.. A.S. grew the Ge/SiGe heterostructure, M.V. supervised the device fabrication and G.S. supervised the heterostructure growth and development. X.Z. and L.M.K.V. conceived the project and L.M.K.V. supervised the project. X.Z., M.R.-R., E.M. and L.M.K.V. wrote the manuscript with inputs from all authors.

Data availability The data reported in this paper are archived on a Zenodo data repository at <https://doi.org/10.5281/zenodo.10431402>

-
- [1] Vandersypen, L. *et al.* Interfacing spin qubits in quantum dots and donors—hot, dense, and coherent. *npj Quantum Inf.* **3**, 34 (2017).
 - [2] Heinrich, A. J. *et al.* Quantum-coherent nanoscience. *Nat. Nanotechnol.* **16**, 1318–1329 (2021).
 - [3] Gonzalez-Zalba, M. *et al.* Scaling silicon-based quantum computing using CMOS technology. *Nat. Electron.* **4**, 872–884 (2021).
 - [4] Chatterjee, A. *et al.* Semiconductor qubits in practice. *Nat. Rev. Phys.* **3**, 157–177 (2021).
 - [5] Stano, P. & Loss, D. Review of performance metrics of spin qubits in gated semiconducting nanostructures. *Nat. Rev. Phys.* **4**, 672–688 (2022).
 - [6] Burkard, G., Ladd, T. D., Pan, A., Nichol, J. M. & Petta, J. R. Semiconductor spin qubits. *Rev. Mod. Phys.* **95**, 025003 (2023).
 - [7] Xue, X. *et al.* Quantum logic with spin qubits crossing the surface code threshold. *Nature* **601**, 343–347 (2022).
 - [8] Noiri, A. *et al.* Fast universal quantum gate above the fault-tolerance threshold in silicon. *Nature* **601**, 338–342 (2022).
 - [9] Mills, A. R. *et al.* Two-qubit silicon quantum processor with operation fidelity exceeding 99%. *Sci. Adv.* **8**, eabn5130 (2022).
 - [10] Hendrickx, N. W. *et al.* A four-qubit germanium quantum processor. *Nature* **591**, 580–585 (2021).
 - [11] Philips, S. G. *et al.* Universal control of a six-qubit quantum processor in silicon. *Nature* **609**, 919–924 (2022).
 - [12] Lawrie, W. *et al.* Simultaneous single-qubit driving of semiconductor spin qubits at the fault-tolerant threshold. *Nat. Commun.* **14**, 3617 (2023).
 - [13] Shulman, M. D. *et al.* Demonstration of entanglement of electrostatically coupled singlet-triplet qubits. *Science* **336**, 202–205 (2012).
 - [14] Nichol, J. M. *et al.* High-fidelity entangling gate for double-quantum-dot spin qubits. *npj Quantum Inf.* **3**, 3 (2017).
 - [15] Weinstein, A. J. *et al.* Universal logic with encoded spin qubits in silicon. *Nature* **615**, 817–822 (2023).
 - [16] Hensgens, T. *et al.* Quantum simulation of a Fermi-Hubbard model using a semiconductor quantum dot array. *Nature* **548**, 70–73 (2017).

- [17] Dehollain, J. P. *et al.* Nagaoka ferromagnetism observed in a quantum dot plaquette. *Nature* **579**, 528–533 (2020).
- [18] van Diepen, C. J. *et al.* Quantum simulation of antiferromagnetic Heisenberg chain with gate-defined quantum dots. *Phys. Rev. X* **11**, 041025 (2021).
- [19] Wang, C.-A. *et al.* Probing resonating valence bonds on a programmable germanium quantum simulator. *npj Quantum Inf.* **9**, 58 (2023).
- [20] Jang, W. *et al.* Individual two-axis control of three singlet-triplet qubits in a micromagnet integrated quantum dot array. *Appl. Phys. Lett.* **117**, 234001 (2020).
- [21] Fedele, F. *et al.* Simultaneous operations in a two-dimensional array of singlet-triplet qubits. *PRX Quantum* **2**, 040306 (2021).
- [22] Mortemousque, P.-A. *et al.* Coherent control of individual electron spins in a two-dimensional quantum dot array. *Nat. Nanotechnol.* **16**, 296–301 (2021).
- [23] Levy, J. Universal quantum computation with spin-1/2 pairs and Heisenberg exchange. *Phys. Rev. Lett.* **89**, 147902 (2002).
- [24] Petta, J. R. *et al.* Coherent manipulation of coupled electron spins in semiconductor quantum dots. *Science* **309**, 2180–2184 (2005).
- [25] Maune, B. M. *et al.* Coherent singlet-triplet oscillations in a silicon-based double quantum dot. *Nature* **481**, 344–347 (2012).
- [26] Wu, X. *et al.* Two-axis control of a singlet–triplet qubit with an integrated micromagnet. *Proc. Natl. Acad. Sci. U.S.A.* **111**, 11938–11942 (2014).
- [27] Jock, R. M. *et al.* A silicon metal-oxide-semiconductor electron spin-orbit qubit. *Nat. Commun.* **9**, 1768 (2018).
- [28] Cerfontaine, P. *et al.* Closed-loop control of a GaAs-based singlet-triplet spin qubit with 99.5% gate fidelity and low leakage. *Nat. Commun.* **11**, 4144 (2020).
- [29] Cerfontaine, P., Otten, R., Wolfe, M., Bethke, P. & Bluhm, H. High-fidelity gate set for exchange-coupled singlet-triplet qubits. *Phys. Rev. B* **101**, 155311 (2020).
- [30] Jirovec, D. *et al.* A singlet-triplet hole spin qubit in planar Ge. *Nat. Mater.* **20**, 1106–1112 (2021).
- [31] Takeda, K. *et al.* Optimized electrical control of a Si/SiGe spin qubit in the presence of an induced frequency shift. *npj Quantum Inf.* **4**, 54 (2018).
- [32] Undseth, B. *et al.* Hotter is easier: Unexpected temperature dependence of spin qubit frequencies. *Phys. Rev. X* **13**, 041015 (2023).
- [33] Undseth, B. *et al.* Nonlinear response and crosstalk of electrically driven silicon spin qubits. *Phys. Rev. Appl.* **19**, 044078 (2023).
- [34] Ono, K., Austing, D., Tokura, Y. & Tarucha, S. Current rectification by pauli exclusion in a weakly coupled double quantum dot system. *Science* **297**, 1313–1317 (2002).
- [35] Qiao, H. *et al.* Floquet-enhanced spin swaps. *Nat. Commun.* **12**, 2142 (2021).
- [36] Chanrion, E. *et al.* Charge detection in an array of CMOS quantum dots. *Phys. Rev. Appl.* **14**, 024066 (2020).
- [37] Duan, J. *et al.* Remote capacitive sensing in two-dimensional quantum-dot arrays. *Nano Lett.* **20**, 7123–7128 (2020).
- [38] Hsiao, T. K. *et al.* Exciton transport in a germanium quantum dot ladder. *arXiv preprint arXiv:2307.02401* (2023).
- [39] Borsoi, F. *et al.* Shared control of a 16 semiconductor quantum dot crossbar array. *Nat. Nanotechnol.* 1–7 (2023).
- [40] Neyens, S. *et al.* Probing single electrons across 300 mm spin qubit wafers. *arXiv preprint arXiv:2307.04812* (2023).
- [41] Scappucci, G. *et al.* The germanium quantum information route. *Nat. Rev. Mater.* **6**, 926–943 (2021).
- [42] Petta, J., Lu, H. & Gossard, A. A coherent beam splitter for electronic spin states. *Science* **327**, 669–672 (2010).
- [43] Ribeiro, H., Petta, J. R. & Burkard, G. Harnessing the GaAs quantum dot nuclear spin bath for quantum control. *Phys. Rev. B* **82**, 115445 (2010).
- [44] Nichol, J. M. *et al.* Quenching of dynamic nuclear polarization by spin-orbit coupling in GaAs quantum dots. *Nat. Commun.* **6**, 7682 (2015).
- [45] Jirovec, D. *et al.* Dynamics of hole singlet-triplet qubits with large g -factor differences. *Phys. Rev. Lett.* **128**, 126803 (2022).
- [46] Mütter, P. M. & Burkard, G. All-electrical control of hole singlet-triplet spin qubits at low-leakage points. *Phys. Rev. B* **104**, 195421 (2021).
- [47] Fernández-Fernández, D., Ban, Y. & Platero, G. Quantum control of hole spin qubits in double quantum dots. *Phys. Rev. Appl.* **18**, 054090 (2022).
- [48] Cai, X., Connors, E. J., Edge, L. F. & Nichol, J. M. Coherent spin–valley oscillations in silicon. *Nature Physics* **19**, 386–393 (2023).
- [49] Rooney, J. *et al.* Gate modulation of the hole singlet-triplet qubit frequency in germanium. *arXiv preprint arXiv:2311.10188* (2023).
- [50] Lodari, M. *et al.* Low percolation density and charge noise with holes in germanium. *Mater. Quantum Technol.* **1**, 011002 (2021).
- [51] Bertrand, B. *et al.* Quantum manipulation of two-electron spin states in isolated double quantum dots. *Phys. Rev. Lett.* **115**, 096801 (2015).
- [52] Hendrickx, N. *et al.* A single-hole spin qubit. *Nat. Commun.* **11**, 3478 (2020).
- [53] Martins, F. *et al.* Noise suppression using symmetric exchange gates in spin qubits. *Phys. Rev. Lett.* **116**, 116801 (2016).
- [54] Reed, M. D. *et al.* Reduced sensitivity to charge noise in semiconductor spin qubits via symmetric operation. *Phys. Rev. Lett.* **116**, 110402 (2016).
- [55] Hendrickx, N. *et al.* Sweet-spot operation of a germanium hole spin qubit with highly anisotropic noise sensitivity. *arXiv preprint arXiv:2305.13150* (2023).
- [56] Hu, X. & Das Sarma, S. Charge-fluctuation-induced dephasing of exchange-coupled spin qubits. *Phys. Rev. Lett.* **96**, 100501 (2006).
- [57] Huang, P., Zimmerman, N. M. & Bryant, G. W. Spin decoherence in a two-qubit CPHASE gate: the critical role of tunneling noise. *npj Quantum Inf.* **4**, 62 (2018).
- [58] Wang, Z. *et al.* Optimal operation points for ultrafast, highly coherent Ge hole spin-orbit qubits. *npj Quantum Inf.* **7**, 54 (2021).
- [59] Wang, C.-A., Scappucci, G., Veldhorst, M. & Russ, M. Modelling of planar germanium hole qubits in electric and magnetic fields. *arXiv preprint arXiv:2208.04795* (2022).
- [60] Massai, L. *et al.* Impact of interface traps on charge noise, mobility and percolation density in Ge/SiGe heterostructures. *arXiv preprint arXiv:2310.05902* (2023).
- [61] Lodari, M. *et al.* Lightly strained germanium quantum wells with hole mobility exceeding one million. *Appl. Phys. Lett.* **120** (2022).

- [62] Stehouwer, L. E. *et al.* Germanium wafers for strained quantum wells with low disorder. *Appl. Phys. Lett.* **123** (2023).
- [63] Dagotto, E. & Rice, T. Surprises on the way from one-to two-dimensional quantum magnets: The ladder materials. *Science* **271**, 618–623 (1996).

Supplementary Information: Universal control of four singlet-triplet qubits

Xin Zhang,^{1,2,*} Elizaveta Morozova,^{1,2,*} Maximilian Rimbach-Russ,^{1,2} Daniel Jirovec,^{1,2}
Tzu-Kan Hsiao,^{1,2} Pablo Cova Fariña,^{1,2} Chien-An Wang,^{1,2} Stefan D. Oosterhout,^{1,3} Amir
Sammak,^{1,3} Giordano Scappucci,^{1,2} Menno Veldhorst,^{1,2} and Lieven M. K. Vandersypen^{1,2,†}

¹*QuTech, Delft University of Technology, Delft, The Netherlands.*

²*Kavli Institute of Nanoscience, Delft University of Technology, Delft, The Netherlands.*

³*Netherlands Organisation for Applied Scientific Research (TNO), Delft, The Netherlands.*

(Dated: December 29, 2023)

This supplementary information includes:

- Supplementary Note [I](#) Experimental setup
- Supplementary Note [II](#) Charge stability diagrams and spin readout
- Supplementary Note [III](#) Virtual gate matrix
- Supplementary Note [IV](#) Asymmetry in measured qubit energy spectrum
- Supplementary Note [V](#) $S-T_0$ and $S-T_-$ oscillations
- Supplementary Note [VI](#) Additional context and data of SWAP operations
- Supplementary Note [VII](#) Pulse scheme and calibration for quantum state transfer
- Supplementary Note [VIII](#) A theoretical model for the SWAP operation

I. EXPERIMENTAL SETUP

A schematic of the measurement setup is shown in Fig. 1. The device is thermally anchored to the mixing chamber of a dilution refrigerator with a base temperature of around 10 mK. All the control electronics are at room temperature, which connect the device via 50 direct current (DC) lines and 24 alternating current (AC) lines in total. The DC and AC signals are combined using bias tees on the printed circuit board (PCB) to apply both signals to the same gate of the device. DC signals are produced by custom-built battery-powered DC voltage sources and are fed through a matrix module—a breakout box with filters inside—to the Fisher cables of the fridge. AC signals are produced by 6 Keysight M3202A modules which are connected directly to the coaxial lines in the fridge. For the filters, we use common-mode Ferrite chokes at room temperature to filter low-frequency noise (10 kHz - 1 MHz) in the ground of AC lines and use RC filters as well as copper-powder filters that are mounted on the cold finger attached to the mixing chamber plate to filter high-frequency noise in DC lines.

The sensing dots are measured using radio-frequency (RF) reflectometry with working frequencies of 179 MHz, 190 MHz, 124 MHz and 158 MHz for sensor S_{TL} , S_{BL} , S_{TR} and S_{BR} , respectively. Tank circuits are formed by NbTiN inductors mounted on the PCB and the spurious capacitance of the bonding wires and metal lines on the board and chip. We apply RF signals using custom-built RF generators and combine them into a single coaxial line at room temperature using a power combiner ZFSC-3-1W-S+. The signal is attenuated at each plate in the dilution refrigerator and passes through a directional coupler (ZEDC-15-2B) at the mixing chamber to reach the device. The signal reflected from the device goes through the same directional coupler and is then amplified with a CITLF3 cryogenic amplifier at the 4K plate. At room temperature, the signal is amplified again and demodulated by custom-built IQ mixers. The demodulated signal is sent to the Keysight M3102A module to convert analog readout signals to digital signals. We use DC blocks to reduce low-frequency noise (< 10 MHz) in the RF lines. The DC block inside the refrigerator blocks the DC signal on the inner conductor (PE8210) while the ones at room temperature block that on both the inner and outer conductor (PE8212). To suppress high-frequency noise in the reflected signal, we use a low-pass filter (SBLP-300+) at room temperature.

* These authors contributed equally to this work

† L.M.K.Vandersypen@tudelft.nl

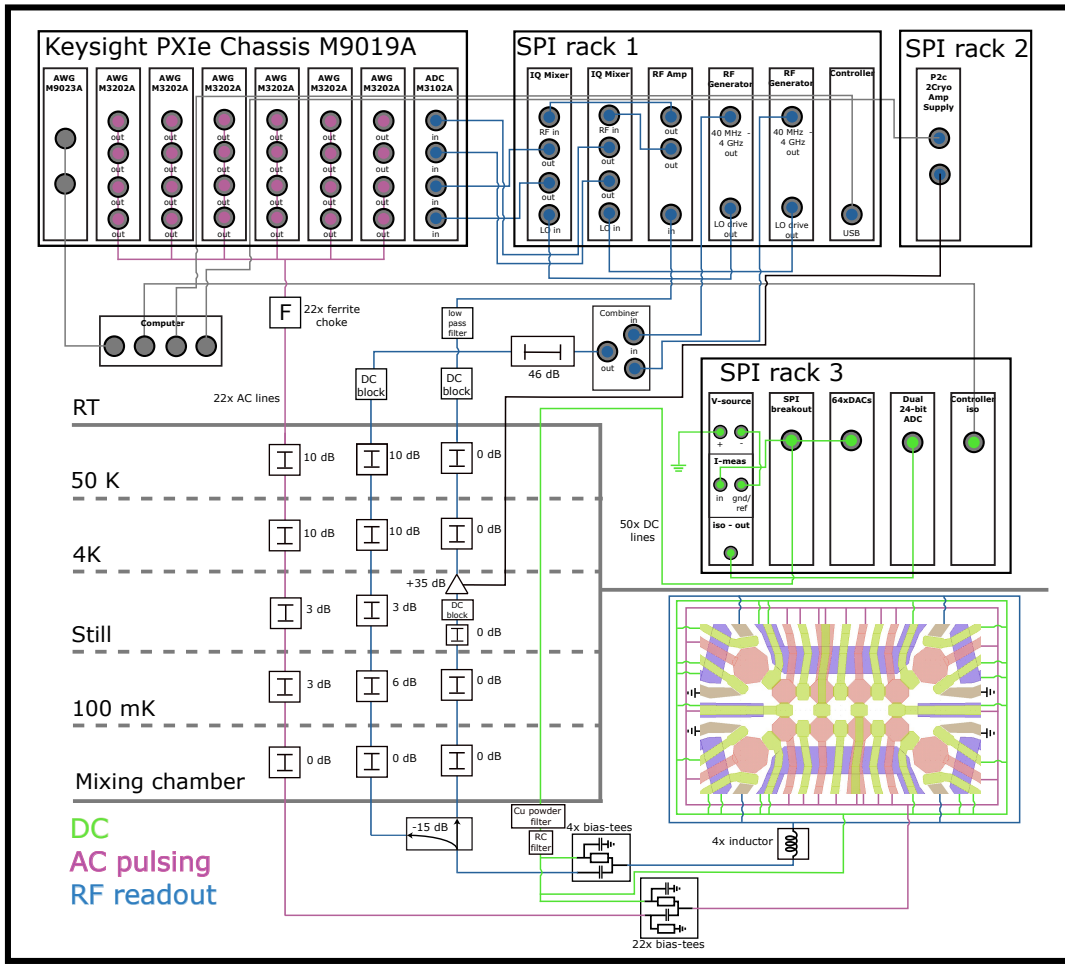


FIG. 1. Measurement circuit for the device. The DC and AC control lines as well as radio-frequency (RF) readout lines are fed from room-temperature instruments to the device at a base temperature of the dilution refrigerator through the cables and various electronic components shown in the figure. The room-temperature instruments include three custom-built SPI racks for supplying DC voltages and RF readout signals, and one Keysight PXIe Chassis for AC pulsing (arbitrary waveform generator, AWG) and data acquisition (analog-to-digital converter, ADC).

II. CHARGE STABILITY DIAGRAMS AND SPIN READOUT

Charge stability diagrams for DQD 1-5, 2-6, 3-7, and 4-8 are shown in Fig. 2a-d, respectively, where we tune all quantum dots to the single-hole regime. To measure the spin states of each DQD, we utilize Pauli-spin blockade (PSB) with diabatic pulses to the readout point [1]. For outer DQD 1-5 and 4-8, as shown by the stability diagram in Fig. 2a and d, we find PSB by pulsing ε_{15} and ε_{48} from (1,1) to (2,0) and (0,2), where within a triangular region an electron tunnels between the dots starting from the $S(1,1)$ but no tunneling occurs (the system is in Pauli spin blockade) from $T_0(1,1)$, $T_-(1,1)$ and $T_+(1,1)$.

As for DQD 2-6 and 3-7, we convert their spin states to those of DQD 5-6 and 7-8 where the sensor signals are stronger. In the following, we take pair 2-6 as an example to explain the readout process of the inner spin pairs. First, we align DQD 1-5 at the charge stability boundary between (2,0) and (2,1), as shown by the white dot in Fig. 2a, and then pulse ε_{26} from negative to positive. We subsequently find a shaded region between (0,1) and (0,2) in the diagram for DQD 2-6, which is caused by PSB in DQD 5-6. The mechanism is shown in Fig. 2e: when we pulse DQD 2-6 to the point where $S(0,2)$ is lower in energy than (0,1), the holes in DQD 2-6 moves across to DQD 5-6, irrespective of the spin states. Subsequently, the conventional PSB mechanism in DQD 5-6 allows $S(1,1)$ to transition to $S(0,2)$, while the triplets $T(1,1)$ have to remain in the (1,1) charge state. In this way, we indirectly realize spin-to-charge conversion for the two spins initially in DQD 2-6. Actually, $S(1,1)$ in DQD 2-6 can also directly tunnel to $S(0,2)$ inside the same DQD, as seen by the curved arrow in Fig. 2e. The mechanism to measure DQD 3-7 is analogous.

In the experiment, we repeatedly perform single-shot readout cycles to obtain singlet or triplet probabilities. The

integration time for each single-shot readout is around 20-40 μs , depending on the signal-to-noise ratio during measurements. To compensate for the drift of the sensor signal, we use a reference readout segment before each measurement sequence [2]. For some datasets, we adjust the single-shot readout threshold by post-processing instead of through a reference segment. In post-processing, we collect a histogram for each data point that includes 1000-4000 shots on which we set the threshold to analyze those shots. In this way, sensor drift between data points is mostly filtered out. The total measurement time needed to collect the data for each 2-dimensional plot in Fig. 1f-i, Fig. 2c-j, Fig. 3d-f and Fig. 4b-c is around 20-40 minutes, using 1000-2000 shots per data point. For the 1-dimensional plot in Fig. 2o and p, the measurement time of each trace is 10-50 minutes with 1000-4000 shots per data point, while for that in Fig. 3g, it is 2 minutes with 1000 shots per data point.

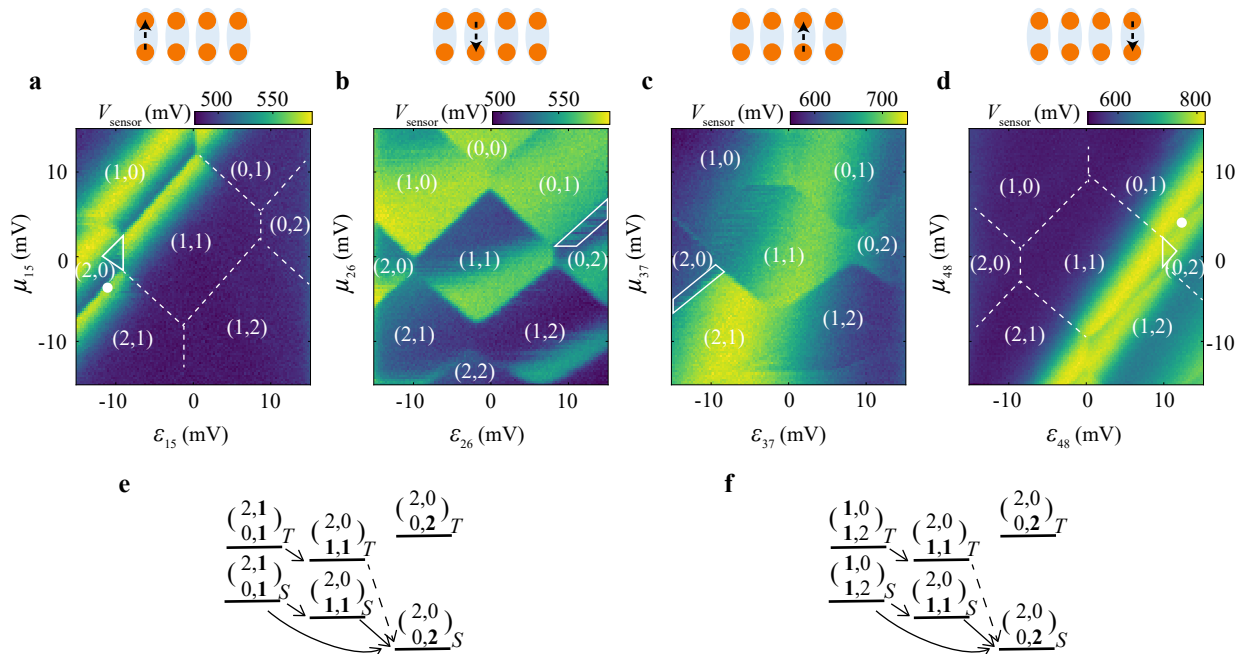


FIG. 2. **a-d**, Charge stability diagrams for DQD 1-5 (**a**), 2-6 (**b**), 3-7 (**c**), and 4-8 (**d**), respectively. **a** and **b** are recorded using the sensor S_{BL} while **c** and **d** are recorded using the sensor S_{BR} . The hole numbers inside the Coulomb blockade region are indicated. The PSB regions are shown by solid white triangles and trapezoids. **e,f**, Illustration of PSB using the energy levels in the quadruple quantum dot plaquette for DQD 2-6 (**e**) and 3-7 (**f**), respectively. The hole numbers are indicated as $(\begin{smallmatrix} n_1 & n_2 \\ n_5 & n_6 \end{smallmatrix})$ for **e** and $(\begin{smallmatrix} n_3 & n_4 \\ n_7 & n_8 \end{smallmatrix})$ for **f**, and the subscript S and T show the two-spin state of holes in the quantum dots indicated by bold numbers, respectively. The solid arrows show fast spin-conserving tunneling while the dashed arrows show suppressed tunneling due to PSB.

III. VIRTUAL GATE MATRIX

As mentioned in the main text, we use virtualized gates to independently control the chemical potential in each quantum dot. The virtual gate matrix is as follows:

$$\begin{pmatrix} vP_1 \\ vP_2 \\ vP_3 \\ vP_4 \\ vP_5 \\ vP_6 \\ vP_7 \\ vP_8 \\ vB_{12} \\ vB_{23} \\ vB_{34} \\ vB_{56} \\ vB_{67} \\ vB_{78} \\ vB_{15} \\ vB_{26} \\ vB_{37} \\ vB_{48} \end{pmatrix} = \begin{pmatrix} 1 & 0.3 & 0.1 & 0.05 & 0.35 & 0.2 & 0.05 & 0.02 & 0.4 & 0.08 & 0 & 0.05 & 0.05 & 0 & 0.4 & 0.15 & 0 & 0 \\ 0.15 & 1 & 0.3 & 0.05 & 0.05 & 0.25 & 0.05 & 0 & 0.3 & 0.2 & 0 & 0.05 & 0.1 & 0 & 0.1 & 0.2 & 0 & 0 \\ 0.05 & 0.25 & 1 & 0.25 & 0 & 0.1 & 0.35 & 0.05 & 0 & 0.15 & 0.06 & 0 & 0.15 & 0.12 & 0 & 0 & 0.08 & 0.07 \\ 0.02 & 0.05 & 0.35 & 1 & 0.02 & 0 & 0.15 & 0.35 & 0 & 0.05 & 0.06 & 0 & 0 & 0.11 & 0 & 0 & 0.03 & 0.28 \\ 0.15 & 0.15 & 0.03 & 0.02 & 1 & 0.25 & 0.05 & 0.03 & 0.1 & 0.05 & 0 & 0.2 & 0.05 & 0.03 & 0.3 & 0 & 0.02 & 0 \\ 0.1 & 0.2 & 0.1 & 0.05 & 0.2 & 1 & 0.2 & 0.05 & 0.1 & 0.1 & 0.05 & 0.1 & 0.25 & 0 & 0.1 & 0.1 & 0 & 0 \\ 0.05 & 0.15 & 0.25 & 0.1 & 0.08 & 0.22 & 1 & 0.15 & 0 & 0.1 & 0.02 & 0.05 & 0.25 & 0.28 & 0.05 & 0 & 0.05 & 0.05 \\ 0 & 0.03 & 0.2 & 0.25 & 0.03 & 0.05 & 0.45 & 1 & 0 & 0.02 & 0.025 & 0.02 & 0.05 & 0.4 & 0 & 0 & 0.03 & 0.22 \\ 0 & 0 & 0 & 0 & 0 & 0 & 0 & 0 & 1 & 0 & 0 & 0 & 0 & 0 & 0 & 0 & 0 & 0 \\ 0 & 0 & 0 & 0 & 0 & 0 & 0 & 0 & 0 & 1 & 0 & 0 & 0 & 0 & 0 & 0 & 0 & 0 \\ 0 & 0 & 0 & 0 & 0 & 0 & 0 & 0 & 0 & 0 & 1 & 0 & 0 & 0 & 0 & 0 & 0 & 0 \\ 0 & 0 & 0 & 0 & 0 & 0 & 0 & 0 & 0 & 0 & 0 & 1 & 0 & 0 & 0 & 0 & 0 & 0 \\ 0 & 0 & 0 & 0 & 0 & 0 & 0 & 0 & 0 & 0 & 0 & 0 & 1 & 0 & 0 & 0 & 0 & 0 \\ 0 & 0 & 0 & 0 & 0 & 0 & 0 & 0 & 0 & 0 & 0 & 0 & 0 & 0 & 1 & 0 & 0 & 0 \\ 0 & 0 & 0 & 0 & 0 & 0 & 0 & 0 & 0 & 0 & 0 & 0 & 0 & 0 & 0 & 1 & 0 & 0 \\ 0 & 0 & 0 & 0 & 0 & 0 & 0 & 0 & 0 & 0 & 0 & 0 & 0 & 0 & 0 & 0 & 1 & 0 \\ 0 & 0 & 0 & 0 & 0 & 0 & 0 & 0 & 0 & 0 & 0 & 0 & 0 & 0 & 0 & 0 & 0 & 1 \end{pmatrix} \begin{pmatrix} P_1 \\ P_2 \\ P_3 \\ P_4 \\ P_5 \\ P_6 \\ P_7 \\ P_8 \\ B_{12} \\ B_{23} \\ B_{34} \\ B_{56} \\ B_{67} \\ B_{78} \\ B_{15} \\ B_{26} \\ B_{37} \\ B_{48} \end{pmatrix}$$

IV. ASYMMETRY IN MEASURED QUBIT ENERGY SPECTRUM

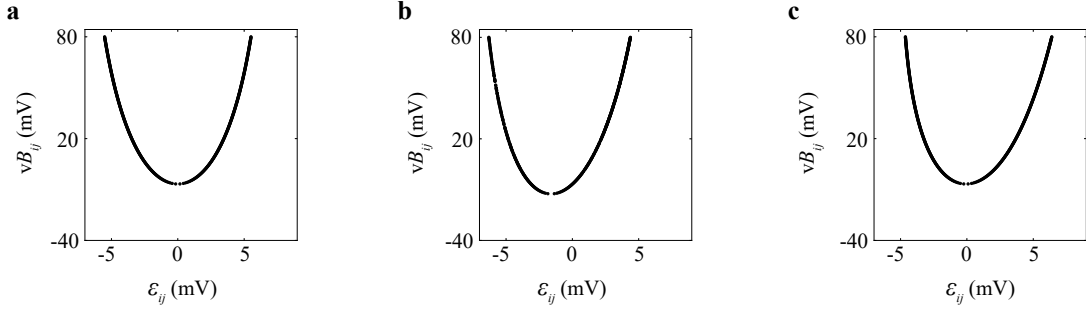


FIG. 3. **a**, Simulated parabola-like curve of the energy spectroscopy as a function of detuning ε_{ij} and barrier voltage vB_{ij} with a standard single-qubit Hamiltonian. **b**, Simulated asymmetrical curve by considering a detuning dependent g -factor. **c**, Simulated asymmetrical curve by considering a linear change of detuning offset as a function of vB_{ij} .

In Fig. 1 of the main text, we show energy spectrums of the $S-T_-$ qubits and mention that the asymmetry of the parabola-like curve may be caused by the detuning-dependent g -factor or an imperfect virtualization of the barrier gate. Here we do a numerical simulation to determine their effects. The results are shown in Fig. 3a-c, which compares the standard energy spectrum (a) with the one with a detuning dependent g -factor (b) and that with imperfect virtualization (c). To numerically simulate these curves, we use the single-qubit Hamiltonian (13) and a relationship of $J = 2t^2U/(U^2 - \varepsilon^2)$. For the parameters, we use $U = 295$ GHz, $\bar{g} = 0.33$, $B = 10$ mT and $\Delta_{ST_-} = 16$ MHz. For the effect of g -factor change, we use a linear change of $\bar{g} = 0.19$ - 0.47 as a function of detuning, while for the effect of imperfect virtualization, we use a linear variation of detuning offset ε_0 as a function of the barrier gate voltage vB_{ij} , which changes in the range of -0.88 - 0.44 mV when vB_{ij} is changed from 80 to -40 mV. The variation of g -factor is a bit far away from the values reported in a similar device, where they report a change of 0.21 - 0.29 as a function of detuning [1]. But the 1% variation of ε_0 is plausible considering the imperfect virtualization. Still, the observed asymmetrical curve in the main text may result from their combined effects.

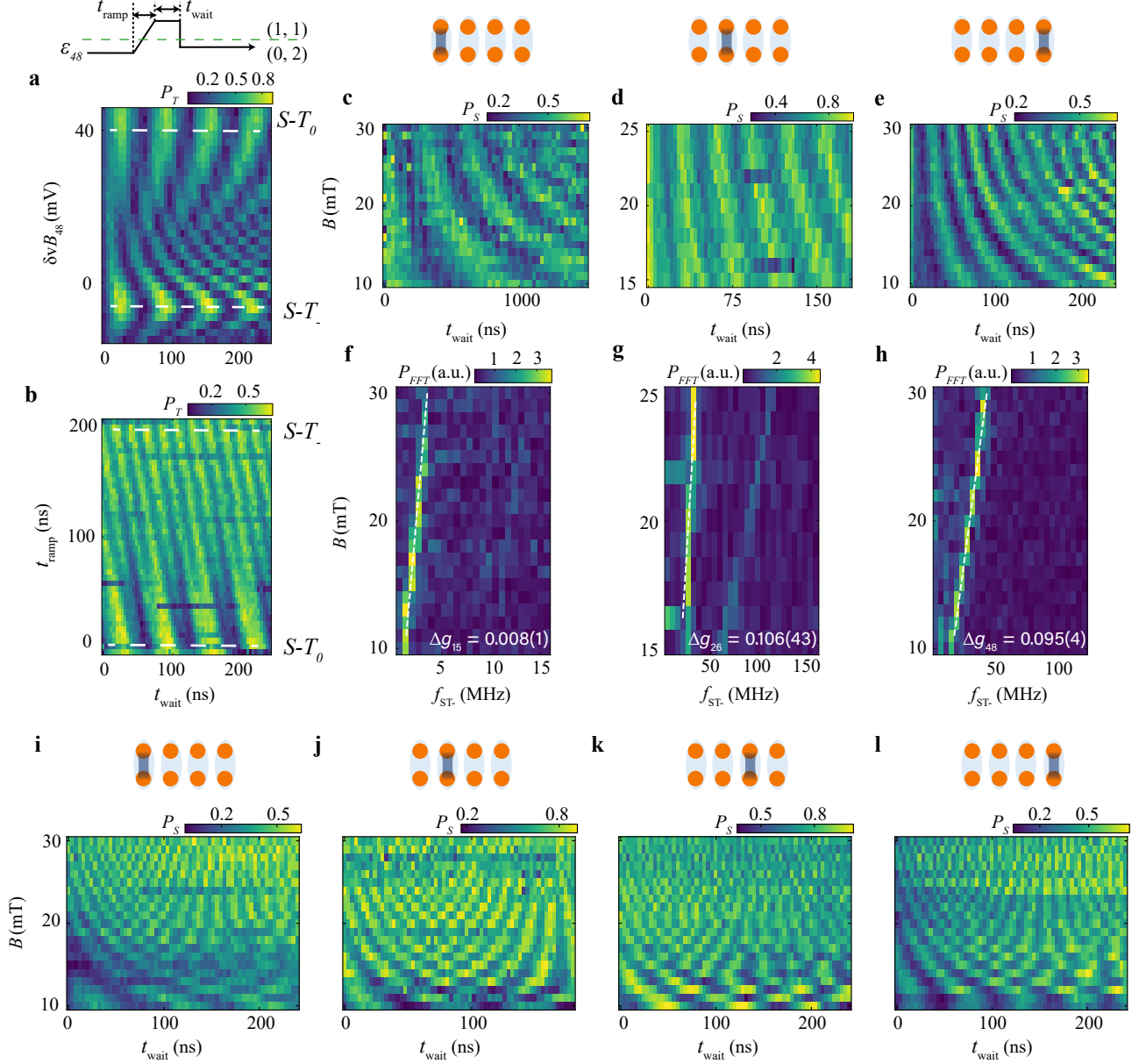
V. $S-T_0$ AND $S-T_-$ OSCILLATIONS

FIG. 4. **a,b**, Measured singlet-triplet oscillations of DQD 4-8 using a square pulse with a ramp-in time t_{ramp} and waiting time t_{wait} . **a**, Measured triplet probabilities as a function of t_{wait} and the barrier voltage amplitude $\delta v B_{48}$ with $t_{\text{ramp}} = 20$ ns. **b**, Measured triplet probabilities as a function of t_{wait} and t_{ramp} with $\delta v B_{48} = 40$ mV. **c-e**, Measured singlet probabilities P_S as a function of t_{wait} and the magnetic field strength B for Q1 (**c**), Q2 (**d**), and Q4 (**e**) under $S-T_0$ control. Here t_{ramp} is set to zero to suppress unwanted $S-T_-$ oscillations. **f-h**, The fast Fourier transforms of the data in **c-e**, with a signal that can be line-fitted using the g -factor difference Δg_{ij} of two dots. **i-l**, Measured singlet probabilities P_S of Q1 (**i**), Q2 (**j**), Q3 (**k**), and Q4 (**l**) as a function of t_{wait} and magnetic field strength B . These qubits are under $S-T_-$ control with $t_{\text{ramp}} = 100$ ns.

In the main text, we discuss the coherent control of $S-T_-$ qubits. Actually, by operating the DQD with different exchange couplings and ramping times, we can also encode a qubit in the $S-T_0$ subspace. Fig. 4a and b use Q4 as an example explaining how we transition from $S-T_-$ to $S-T_0$ oscillations. As mentioned in the main text, a block pulse with 20-nanosecond ramp time (t_{ramp}) from (0,2) to (1,1) is adiabatic with respect to the $S-T_0$ splitting but

nonadiabatic with respect to the $S-T_-$ anticrossing. Therefore, we can drive x -rotations of $S-T_-$ qubits when this pulse amplitude reaches the detuning center where $J(\varepsilon_{ij} = 0) \sim \overline{E}_z$ (see Fig. 1d in the main text). However, when we increase the barrier voltage change $\delta v B_{48}$ until $J(\varepsilon_{ij} = 0) < \overline{E}_z$ (see Fig. 1c in the main text), the $S-T_-$ anticrossings are no longer at the detuning center, therefore the same pulse cannot produce the x -axis oscillations of $S-T_-$ qubits. Moreover, under this condition, the energy gap of the $S-T_0$ splitting is reduced and the 20-nanosecond ramp time is no longer adiabatic with respect to the $S-T_0$ splitting. As a result, the singlet state will nutate between the S and T_0 states under the control of the Zeeman energy difference between the two dots ΔE_z . The corresponding experimental result is shown in Fig. 4a, where we can observe clear $S-T_-$ oscillations with $\delta v B_{48} \sim -10$ mV and $S-T_0$ oscillations with $\delta v B_{48} \sim 40$ mV.

This crossover between $S-T_-$ and $S-T_0$ oscillations can also be tuned by changing t_{ramp} . At $\delta v B_{48} = 40$ mV, when we increase t_{ramp} until the pulse is adiabatic again with respect to the $S-T_0$ splitting, the $S-T_0$ oscillations can no longer be observed. However, such a long ramp time can rotate the initial state and make z -axis control of $S-T_-$ qubits visible again [3]. Therefore, we also observe a transition of $S-T_0$ oscillations and $S-T_-$ oscillations as a function of t_{ramp} in experiments. As shown in Fig. 4b, $S-T_0$ oscillations disappear and $S-T_-$ oscillations are recovered when t_{ramp} surpasses 100 ns.

Using the method above, we measured $S-T_0$ oscillations as a function of the magnetic field with $t_{\text{ramp}} = 0$ ns for Q1, Q2, and Q4, as shown in Fig. 4c-e. The corresponding fast Fourier transforms (FFT) are shown in Fig. 4(f-h), from which we extract g -factor differences Δg as 0.008(1), 0.106(43), and 0.095(4) for Q1, Q2, and Q4, respectively. For Q3, we didn't find $S-T_0$ oscillations, which may be because the corresponding Δg is too low to detect. We also measured $S-T_-$ oscillations as a function of the magnetic field with $t_{\text{ramp}} = 100$ ns for Q1-Q4, as shown in Fig. 4i-l, and extract $\bar{g} = 0.33(1) - 0.37(1)$ (see Fig. 2m in the main text).

VI. ADDITIONAL CONTEXT AND DATA OF SWAP OPERATIONS

For the SWAP interaction of Q3-Q4, we also scanned the oscillations over a wider range of detuning compared to the data of Fig. 3f in the main text. The result is shown in Fig. 5a. There are three sets of oscillations from left to right, where the rightmost corresponds to SWAP oscillations of Q3-Q4 discussed in the main text, the middle oscillations correspond to a single-qubit operation of Q4, and the leftmost is also a set of SWAP oscillations but with a very slow oscillation speed, which corresponds to a smaller interqubit coupling than the rightmost one due to the detuning arrangement (see the leftmost anticrossing in Fig. 3b of the main text). These features can all be qualitatively understood using Fig. 3b in the main text. However, to quantitatively simulate its behavior, the contribution of anisotropic exchange couplings may be needed.

We also tried sequential readout after SWAP oscillations of Q2-Q3. By pulsing the barrier gate $\delta v B_{26}$ to -60 mV, we can measure Q3 (during 20 μ s) and simultaneously keep Q2 in the center of (1,1) with sufficiently large J , where the Hamiltonian eigenbasis corresponds to the qubit readout basis [2, 4, 5]. Afterwards, Q2 is measured in the same sequence. Thus, the two-qubit joint probabilities P_{SS} , P_{TS} , P_{ST} and P_{TT} of Q2 and Q3, can be acquired simultaneously. By initializing Q2-Q3 into $|T_-S\rangle$, we observe out-of-phase oscillations of P_{TS} and P_{ST} under SWAP interactions in Fig. 5b. For comparison, if Q2-Q3 is initialized into $|SS\rangle$, we do not observe any oscillations, as expected, except for the single-qubit rotations at low detuning, as shown in Fig. 5c. We don't observe leakage to $|TT\rangle$, which is expected given that, in this regime, the states $|TT\rangle$ are far away in energy from the other states, see Fig. 3b in the main text.

VII. PULSE SCHEME AND CALIBRATION FOR QUANTUM STATE TRANSFER

The detailed pulse scheme for quantum state transfer in the main text is shown in Fig. 6a. We initialize Q1-Q4 in the $\begin{pmatrix} 2 & 0 & 2 & 0 \\ 0 & 2 & 0 & 2 \end{pmatrix}$ regime and then diabatically pulse to the $\begin{pmatrix} 1 & 1 & 1 & 1 \\ 1 & 1 & 1 & 1 \end{pmatrix}$ regime, preserving four singlets. At this point, the detuning of Q1 and Q3 is set close to the (1,1)-(2,0) transition and that of Q4 close to the (1,1)-(0,2) transition in order to stay away from the $S-T_-$ anticrossing. This ensures that these three qubits remain in the singlet state. The detuning of Q2 is set to zero such that Q2 rotates around its x axis to $|T_-$). Then we pulse the detunings and barrier gates of Q1-Q2 to initiate a SWAP interaction for a duration t_{wait} , after which we transfer the state of Q2 to Q4 by performing sequential SWAP operations of Q2-Q3 and Q3-Q4. Finally, we pulse Q4 to zero detuning to kickstart single-qubit evolution around the x -axis for a duration t_{Q4} . For readout, we pulse Q1-Q4 into $\begin{pmatrix} 1 & 1 & 1 & 0 \\ 1 & 1 & 1 & 0 \end{pmatrix}$ where we perform PSB readout of Q4. The detunings of Q1-Q3 are set to zero while Q4 is read out, but this will not affect the readout since Q4 is protected by a very large J in the readout window.

Before the quantum state transfer experiment, we confirm the operation of the individual SWAP gates by performing a single-qubit rotation of one qubit and measuring its state using the other after a SWAP gate. Some results are

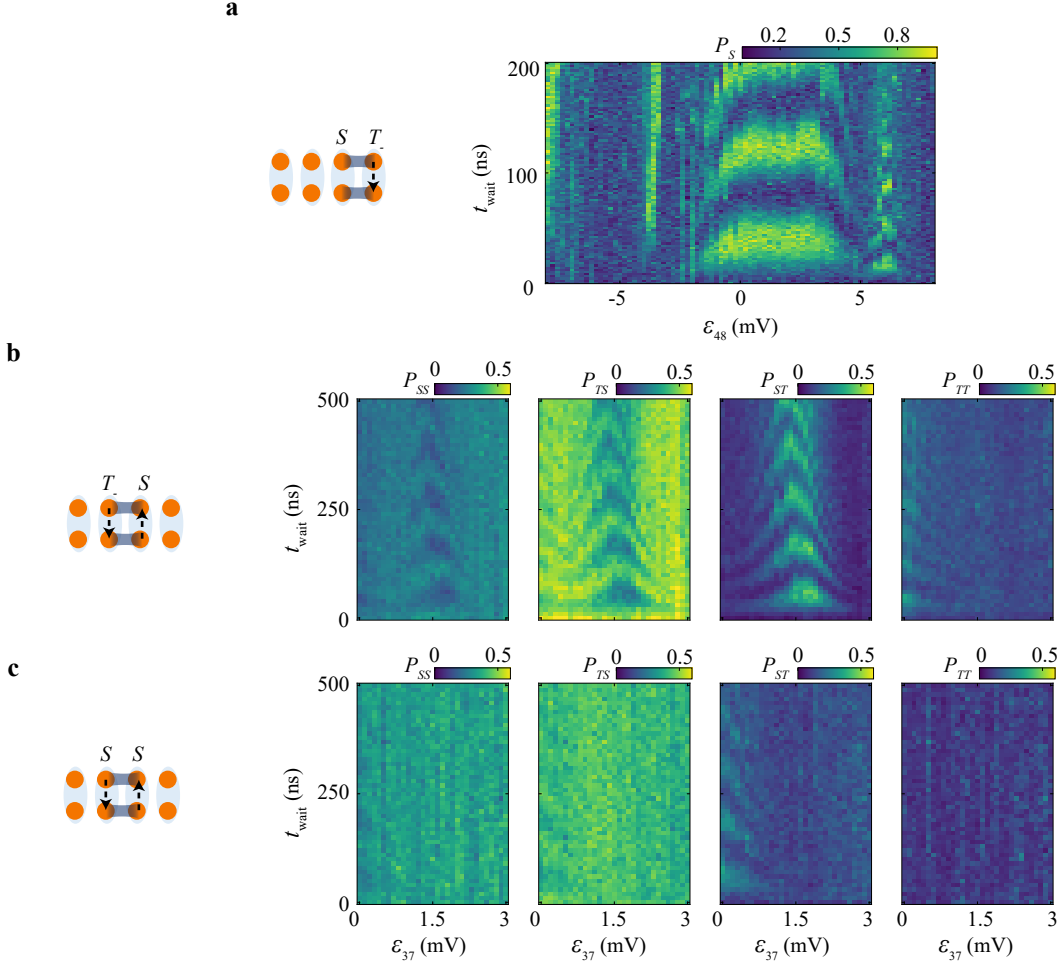


FIG. 5. **a**, Measured triplet probabilities of Q4 as a function of waiting time t_{wait} and the detuning of Q4, ϵ_{48} , after initializing Q3-Q4 into $|ST_{-}\rangle$. **b,c**, Sequentially measured probabilities P_{SS} , P_{TS} , P_{ST} and P_{TT} of Q2 and Q3 as a function of t_{wait} and the detuning of Q3, ϵ_{37} , after initializing Q2-Q3 into $|T_{-}S\rangle$ (**b**) and $|SS\rangle$ (**c**). The data is acquired at a different magnetic field $B = 5$ mT but the detuning arrangement is similar to the results in the main text. In **b**, the out-of-phase signals in P_{TS} and P_{ST} observed around $\epsilon_{37} = 1.5$ mV are the result of the SWAP oscillations between these two qubits. A similar signal to P_{TS} but with lower visibility is observed in P_{SS} , which can be explained by the higher triplet readout error for Q2 than for Q3.

shown in Fig. 6b and c, where we perform this test for Q3-Q4 and Q2-Q3, respectively. Fig. 6d shows a result where Q1 is rotated and the measured qubit is Q4 following three consecutive SWAP gates from Q1 to Q4. A comparison of the direct readout of Q1 is shown in Fig. 6e, with similar oscillations to that of Fig. 6d at similar detuning voltages. These results demonstrate the SWAP gates are of sufficient quality to allow quantum state transfer across the entire array.

VIII. A THEORETICAL MODEL FOR THE SWAP OPERATION

Holes confined in quantum dots are well described by the conventional Fermi-Hubbard model [6]. In the presence of a finite magnetic field and spin-orbit interaction, the Fermi-Hubbard model can be written as

$$\begin{aligned}
 H_{\text{FH}} = & \sum_{i=1} \left[\mu_i n_i + \mu_B \mathbf{B} \cdot \tilde{\mathcal{G}}_i \mathbf{S}_i \right] + \sum_{i=1} \frac{\tilde{U}_i}{2} n_i (n_i - 1) + \sum_{\langle i,j \rangle} V_{ij} n_i n_j \\
 & + \sum_{\sigma=\uparrow,\downarrow} \left(\tilde{t}_{ij} c_{i,\sigma}^\dagger c_{j,\sigma} + \text{h.c.} \right) + \sum_{\sigma=\uparrow,\downarrow} \left(\tilde{t}_{\text{SO},ij} c_{i,\sigma}^\dagger c_{j,\bar{\sigma}} + \text{h.c.} \right). \quad (1)
 \end{aligned}$$

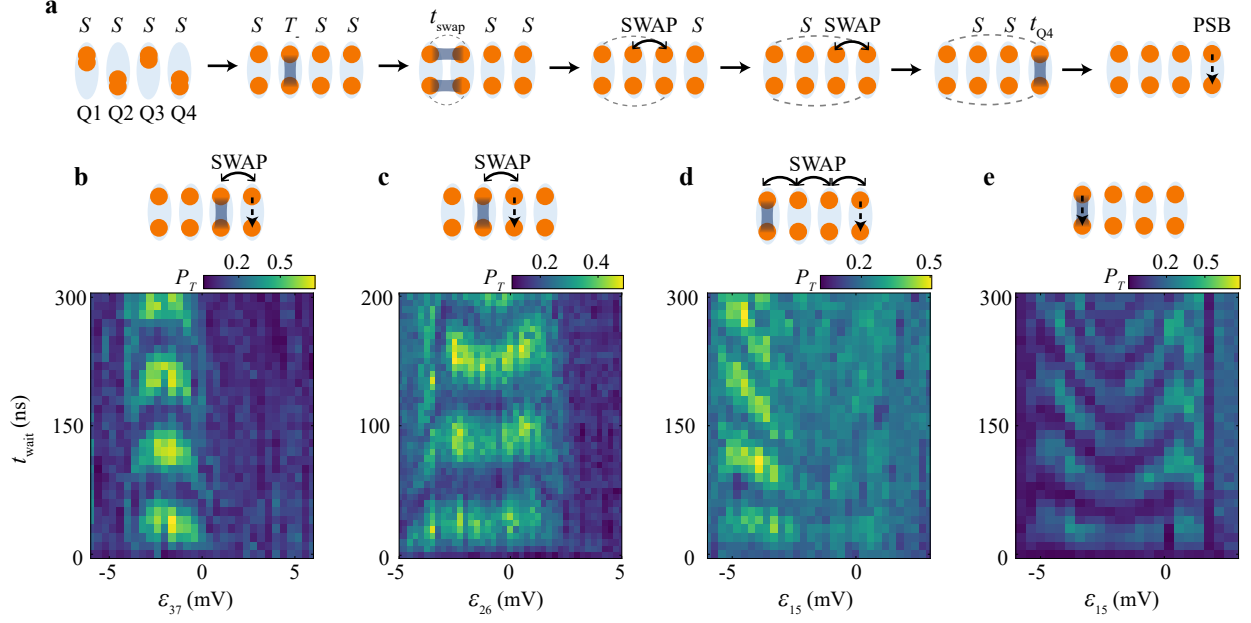


FIG. 6. **a**, Schematic representation of the different steps in the quantum-state-transfer experiment of Fig. 4 of the main text. The gray dashed curves indicate potential entanglement between two qubits. The black curved double-arrow refers to a SWAP gate that is intended to transfer information from one qubit to the next. **b**, Measured triplet probabilities of Q4 as a function of waiting time t_{wait} and detuning of Q3, ϵ_{37} . The inset illustrates that we control Q3 to perform an x -rotation with a time t_{wait} and subsequently perform a SWAP gate of Q3-Q4 and measure Q4 using PSB. **c**, Measured triplet probabilities of Q3 as a function of t_{wait} and detuning of Q2, ϵ_{26} . The inset illustration is similar to that in **b** but with single-qubit control of Q2, a subsequent SWAP gate of Q2-Q3 and PSB measurement of Q3. **d**, Measured triplet probabilities of Q4 as a function of t_{wait} and the detuning of Q1, ϵ_{15} . The inset shows that we perform an x -rotation of Q1 with a time t_{wait} followed by three consecutive SWAP gates to transfer the state of Q1 to Q2, Q3 and Q4, after which we measure Q4 using PSB. **d** has lower visibility on the right-hand side of the figure compared to its left-hand side, which can be attributed to a possible parameter shift of the consecutive SWAP gates by low-frequency charge noise after the left part was scanned. **e**, Direct readout of Q1 with the same single-qubit control as in **d**.

Here, h.c. denotes hermitian conjugate, $\bar{\sigma}$ the opposite spin state of σ , the operator $c_{i,\sigma}^\dagger$ ($c_{i,\sigma}$) creates (annihilates) a hole in QD i with spin $\sigma = \uparrow, \downarrow$, $n_i \equiv \sum_{\sigma} c_{i,\sigma}^\dagger c_{i,\sigma}$ is the charge number operator, and $\mathbf{S} = (S_{x,i}, S_{y,i}, S_{z,i})^T$ is the vector consisting of the spin matrices

$$S_{x,i} = \frac{\hbar}{2}(c_{i,\uparrow}^\dagger c_{i,\downarrow} + c_{i,\downarrow}^\dagger c_{i,\uparrow}) \quad (2)$$

$$S_{y,i} = -i\frac{\hbar}{2}(c_{i,\uparrow}^\dagger c_{i,\downarrow} - c_{i,\downarrow}^\dagger c_{i,\uparrow}) \quad (3)$$

$$S_{z,i} = \frac{\hbar}{2}(c_{i,\uparrow}^\dagger c_{i,\uparrow} - c_{i,\downarrow}^\dagger c_{i,\downarrow}). \quad (4)$$

The first line in Hamiltonian (1) describes the hole energies, i.e., μ_i denotes the chemical potential in QD i , \tilde{U}_i is the Coulomb repulsion for doubly occupying the i -th QD, V_{ij} is the Coulomb repulsion of two holes occupying neighboring QDs i and j , μ_B is Bohr's magneton, and \tilde{G}_i is the quantum dot g-tensor. The second line describes the hopping terms between neighboring sites denoted by the spin-conserving tunnel matrix elements \tilde{t}_{ij} and spin-non-conserving tunnel matrix elements $\tilde{t}_{\text{SO},ij}$. Note, that this notation is consistent with Refs. [7, 8] as \tilde{t}_{ij} and $\tilde{t}_{\text{SO},ij}$ can be complex in general.

Single-qubit Hamiltonian

Considering only two neighboring quantum dots, the Hamiltonian can be simplified by transforming into the spin-orbit frame [8]. Intuitively, since the spin-orbit interaction only rotates the spin during tunneling, local spin rotations

can always “unwind” the rotation. As a consequence of the spin-orbit interaction, the g-tensor of quantum dot i is rotated as $\tilde{\mathcal{G}}_i \rightarrow R_i \tilde{\mathcal{G}}_i \equiv \mathcal{G}_i$, and the tunnel coupling is renormalized as $t = \sqrt{|\tilde{t}|^2 + |\tilde{t}_{\text{SO}}|^2}$ [8].

Hamiltonian The respective Hamiltonian in the basis $\{S(2,0), S(0,2), S(1,1), T_-(1,1), T_0(1,1), T_+(1,1)\}$ of the spin-orbit frame reads

$$H_{\text{DQD}} = \begin{bmatrix} U + \varepsilon & 0 & \sqrt{2}t & 0 & 0 & 0 \\ 0 & U - \varepsilon & \sqrt{2}t & 0 & 0 & 0 \\ \sqrt{2}t & \sqrt{2}t & 0 & \frac{\Delta E_x - i\Delta E_y}{\sqrt{2}} & \Delta E_z & -\frac{\Delta E_x + i\Delta E_y}{\sqrt{2}} \\ 0 & 0 & \frac{\Delta E_x + i\Delta E_y}{\sqrt{2}} & -\bar{E}_z & \frac{\bar{E}_x + i\bar{E}_y}{\sqrt{2}} & 0 \\ 0 & 0 & \Delta E_z & \frac{\bar{E}_x - i\bar{E}_y}{\sqrt{2}} & 0 & \frac{\bar{E}_x + i\bar{E}_y}{\sqrt{2}} \\ 0 & 0 & -\frac{\Delta E_x + i\Delta E_y}{\sqrt{2}} & 0 & \frac{\bar{E}_x - i\bar{E}_y}{\sqrt{2}} & \bar{E}_z \end{bmatrix}. \quad (5)$$

Here, we introduce the energy detuning $\varepsilon = \mu_1 - \mu_2$, and the average and difference in Zeeman energy for a fixed magnetic field direction, $2\hat{E}_\xi = \mu_B \mathbf{B}(\mathcal{G}_1 + \mathcal{G}_2)\hat{\xi}$ and $2\Delta E_\xi = \mu_B \mathbf{B}(\mathcal{G}_1 - \mathcal{G}_2)\hat{\xi}$, where $\hat{\xi}$ is the unit vector along axis $\xi = x, y, z$. We note that in our experiment we only have access to the energies and not the individual g-tensors due to the lack of access to a vector magnet.

Simulations To compute the single-qubit energy spectra in the main text (Fig. 1c-e), we use Hamiltonian (1) assuming only real tunnel matrix elements. Explicitly, we set the spin-conserving tunneling as $\tilde{t} = 1.2, 1.86, 2.4$ GHz, the spin-non-conserving tunneling as $\tilde{t}_{\text{SO}} = 10$ MHz, and $U = 300$ GHz, $B = |\mathbf{B}| = 10$ mT, $\bar{g} = |\mathcal{G}_1 + \mathcal{G}_2|/2 = 0.33$, $\Delta g = |\mathcal{G}_1 - \mathcal{G}_2|/2 = 0.008$, and with all other components of the g-tensors set to zero.

Effective qubit Hamiltonian To separate the spin dynamics from the charge dynamics, we now restrict ourselves to the subspace spanned by the spin states $\{S(1,1), T_-(1,1), T_0(1,1), T_+(1,1)\}$. This can be done either by block-diagonalizing via Schrieffer-Wolff perturbation theory [9] or by diagonalizing the singlet sector spanned by $\{S(2,0), S(0,2), S(1,1)\}$ with a subsequent projection or block-diagonalization [8]. Regardless of the chosen method, the resulting Hamiltonian has the form of a generalized Heisenberg Hamiltonian

$$H_{\text{DQD}} = \begin{bmatrix} J_0 & \frac{\Delta E_x - i\Delta E_y}{\sqrt{2}} & \Delta E_z & -\frac{\Delta E_x + i\Delta E_y}{\sqrt{2}} \\ \frac{\Delta E_x + i\Delta E_y}{\sqrt{2}} & -\bar{E}_z & \frac{\bar{E}_x + i\bar{E}_y}{\sqrt{2}} & 0 \\ \Delta E_z^* & \frac{\bar{E}_x - i\bar{E}_y}{\sqrt{2}} & 0 & \frac{\bar{E}_x + i\bar{E}_y}{\sqrt{2}} \\ -\frac{\Delta E_x + i\Delta E_y}{\sqrt{2}} & 0 & \frac{\bar{E}_x - i\bar{E}_y}{\sqrt{2}} & \bar{E}_z \end{bmatrix}, \quad (6)$$

where J_0 is the exchange interaction. In the regime of single dot occupation, $|t| \ll |U \pm \varepsilon|$, the exchange interaction can be approximated by [9]

$$J = \frac{2t^2U}{U^2 - \varepsilon^2}. \quad (7)$$

We note that during the transformation $\Delta E_{x,y,z} \rightarrow \Delta E'_{x,y,z}$ is renormalized by the charge-state admixture [8, 10]. To improve readability and because it has no practical consequences, we immediately drop the prime.

Starting from Hamiltonian (6) we can now construct the qubit Hamiltonian. The $|0\rangle \equiv |S\rangle = S(1,1)$ qubit state is defined via the PSB readout mechanism. We find the second qubit state by diagonalizing the triplet sector spanned by $\{T_-(1,1), T_0(1,1), T_+(1,1)\}$. Fortunately, the transformation can be parameterized as $e^{-i\mathbf{v}\cdot\mathbf{S}^0/\hbar}$, where \mathbf{v} is a real vector and \mathbf{S}^0 is a vector containing the spin-0 matrices

$$S_x^0 = \frac{1}{2}(S_{x,1} + S_{x,2}) \quad (8)$$

$$S_y^0 = \frac{1}{2}(S_{y,1} + S_{y,2}) \quad (9)$$

$$S_z^0 = \frac{1}{2}(S_{z,1} + S_{z,2}). \quad (10)$$

The $|1\rangle \equiv |T_-\rangle$ qubit state is then consequently given by the lowest-energy state. The final qubit Hamiltonian reads

$$\tilde{H}_{ST_-} = \begin{bmatrix} -J & \frac{\Delta_{ST_-} e^{i\phi_{ST_-}}}{2} \\ \frac{\Delta_{ST_-} e^{-i\phi_{ST_-}}}{2} & -\bar{E}_z \end{bmatrix}. \quad (11)$$

In lowest-order perturbation theory the exchange energy $J = J_0$, the average Zeeman splitting $\bar{E}_z = \sqrt{\bar{E}_x^2 + \bar{E}_y^2 + \bar{E}_z^2}$, and the spin-orbit coupling reads

$$\Delta_{\text{SO}} e^{i\phi_{ST_-}} = \sqrt{2} \frac{\Delta E_z (\bar{E}_x^2 + \bar{E}_y^2) - \bar{E}_z (\Delta E_x \bar{E}_x + \Delta E_y \bar{E}_y)}{\bar{E}_z (\hat{E}_x - i\bar{E}_y)} + \sqrt{2} i \frac{\Delta E_x \bar{E}_y - \Delta E_y \bar{E}_x}{(\hat{E}_x - i\bar{E}_y)}. \quad (12)$$

To arrive at the single-qubit Hamiltonian in the main text, we apply the local phase transformation $U_\phi = \exp(-i\phi_{ST_-}(|0\rangle\langle 0| - |1\rangle\langle 1|)/2)$

$$H_{ST_-} = U_\phi \tilde{H}_{ST_-} U_\phi^\dagger = \begin{bmatrix} -J & \frac{\Delta_{ST_-}}{2} \\ \frac{\Delta_{ST_-}}{2} & -\bar{E}_z \end{bmatrix}, \quad (13)$$

We remark that a more accurate Hamiltonian can be computed recursively using perturbation theory for a sufficiently large spectral gap [11]. We also remark that leakage outside the qubit subspace can be strongly suppressed using optimal control theory and Hamiltonian engineering.

Decoherence times

Charge noise and nuclear spin noise are ubiquitous in germanium semiconductor devices. Due to the low-frequency nature of both types of noise, they can be approximately modeled as quasistatic fluctuations of input parameters, giving rise to pure dephasing. Furthermore, we ignore in our analysis any energy relaxation mechanism, which is a good approximation for spin qubits [6]. Hamiltonian (13) under weak low-frequency noise thus becomes [12]

$$H_{ST_-} = \begin{bmatrix} -J - \delta J & \frac{\Delta_{ST_-} + \delta\Delta_x - i\delta\Delta_y}{2} \\ \frac{\Delta_{ST_-} + \delta\Delta_x + i\delta\Delta_y}{2} & -\bar{E}_z - \delta\bar{E}_z \end{bmatrix}, \quad (14)$$

where δ denotes fluctuations. Note that there are two off-diagonal contributions $\delta\Delta_x$ and $\delta\Delta_y$ that arise from the complex quantity $\Delta_{ST_-} e^{i\phi_{ST_-}}$. Assuming quasi-static noise (or low-frequency noise within the adiabatic approximation) the qubit resonance frequency is modulated by noise as follows

$$\hbar\omega_q = \sqrt{4(J - \bar{E}_z)^2 + \Delta_{ST_-}^2} \rightarrow \sqrt{4(J - \bar{E}_z + \delta J - \delta\bar{E}_z)^2 + (\Delta_{ST_-} + \delta\Delta_x)^2 + \delta\Delta_y^2}. \quad (15)$$

The $S-T_-$ qubit is operated in two regimes which we separately discuss.

Dephasing during rotations around the x-axis For single-qubit x -rotations, we operate at $J = \bar{E}_z$ and we can expand Eq. (15) up to first order

$$\hbar\omega_q^x = \Delta_{ST_-} + \delta\Delta_x + \mathcal{O}(\delta^2) \quad (16)$$

to find the dominating contributions. Assuming Gaussian distributed noise, the decoherence time in the x -axis rotation regime is then given by

$$T_x^* = \frac{1}{\sqrt{2}\sigma_{\Delta_x}}, \quad (17)$$

where $\sigma_{\Delta_x}^2 = \langle \delta\Delta_x^2 \rangle - \langle \delta\Delta_x \rangle^2$ is the standard deviation of the $\delta\Delta_x$ noise. Since $\Delta E_\xi \propto B$ and $\bar{E}_\xi \propto B$ for $\xi = x, y, z$, we expect $T_x^* \propto B^{-1}$ for an in-plane magnetic field [13, 14]. Therefore, operating at small magnetic fields is beneficial for x -gates.

Dephasing during rotations around the z-axis For single-qubit z -rotations, we operate at $|J - \bar{E}_z| \gg \Delta_{ST_-}$ and we can expand Eq. (15) up to first order

$$\hbar\omega_q^z = |J - \bar{E}_z + \delta J - \delta\bar{E}_z| + \mathcal{O}(\delta^2) \quad (18)$$

to find the dominating contributions. Assuming Gaussian distributed noise the decoherence time in the z -axis rotation regime is then given by

$$T_z^* = \frac{1}{\sqrt{2}\sigma_{J, \bar{E}_z}(1 + c)}, \quad (19)$$

where $\sigma_{\sigma_J, \bar{E}_z}^2 = \langle (\delta J - \delta \bar{E}_z)^2 \rangle - \langle (\delta J - \delta \bar{E}_z) \rangle^2$ is the standard deviation of the noise difference, $c = \text{cov}(J, \bar{E}_z) / (\sigma_J \sigma_{\bar{E}_z})$ the noise correlation factor, $\text{cov}(J, \bar{E}_z)$ the covariance, and σ_J ($\sigma_{\bar{E}_z}$) the standard deviation of the individual fluctuations δJ and $\delta \bar{E}_z$. Since $\bar{E}_z \propto B$, operating at small magnetic fields can suppress fluctuations of the Zeeman splitting, giving rise to $T_z^* = \frac{1}{\sqrt{2}\sigma_J}$. In contrast to T_x^* , thus, T_z^* is not suppressed at small magnetic fields. This is consistent with the observations in the main text that $T_z^* < T_x^*$.

Two-qubit Hamiltonian

The derivation of the Hamiltonian of two coupled S - T_- qubits is analogous to that of the single-qubit Hamiltonian. The first step is separating the spin and charge degree of freedom, resulting in a generalized Heisenberg Hamiltonian. We give explicit expressions for the two-qubit Hamiltonian for two different architectures, a simplified architecture with single connectivity and the design from the experiment.

Linear chain with a single inter-qubit tunnel (exchange) coupling and isotropic g-tensor up to a scaling. In this case, the multi-qubit Hamiltonian is given by

$$H_{\text{FH}} = \sum_{i=1} \mu_B g_i B S_{z,i} + \sum_{i=1} \frac{\Delta_{ST-,i}}{\hbar} S_x + \sum_{\langle i,j \rangle} J_{ij} \left(\frac{\mathbf{S}_i \cdot \mathbf{S}_j}{\hbar^2} - \frac{1}{4} \right), \quad (20)$$

where $\langle i, j \rangle$ denotes neighboring quantum dots. Projected on the two-qubit basis $\{|S, S\rangle, |S, T_-\rangle, |T_-, S\rangle, |T_-, T_-\rangle\}$ the two-qubit Hamiltonian reads

$$H_{2\text{Q}} = H_{\text{Q1}} + H_{\text{Q2}} + H_{\text{coup,iso}} \quad (21)$$

with

$$H_{\text{Q1}} + H_{\text{Q2}} = \begin{bmatrix} -J_{ij} - J_{kl} & \frac{\Delta_{\text{SO},kl}}{2} & \frac{\Delta_{\text{SO},ij}}{2} & 0 \\ \frac{\Delta_{\text{SO},kl}}{2} & -J_{ij} - \bar{E}_{z,kl} & 0 & \frac{\Delta_{\text{SO},ij}}{2} \\ \frac{\Delta_{\text{SO},ij}}{2} & 0 & -\bar{E}_{z,ij} - J_{kl} & \frac{\Delta_{\text{SO},kl}}{2} \\ 0 & \frac{\Delta_{\text{SO},ij}}{2} & \frac{\Delta_{\text{SO},kl}}{2} & -\bar{E}_{z,ij} - \bar{E}_{z,kl} \end{bmatrix}, \quad (22)$$

$$H_{\text{coup,iso}} = \frac{1}{2} \begin{bmatrix} -J_{\text{coup}} & 0 & 0 & 0 \\ 0 & -J_{\text{coup}} & J_{\text{coup}} & 0 \\ 0 & J_{\text{coup}} & -J_{\text{coup}} & 0 \\ 0 & 0 & 0 & 0 \end{bmatrix}, \quad (23)$$

Here the subscripts indicate the sites i, j, k and l , respectively. Note that this Hamiltonian is identical to the Hamiltonian used in the main text up to an energy offset that corresponds to a global phase shift.

From a quantum information point of view, the isotropic exchange Hamiltonian (23) generates a universal two-qubit gate. More precisely, the Hamiltonian generates a SWAP + iSWAP gate. This can be visualized through the symmetry of the system: since the isotropic exchange interaction is given by the projector on the singlet subspace, the $|T_-, T_-\rangle \langle T_-, T_-|$ matrix element of the two-qubit interaction has to be zero.

Ladder with two inter-qubit tunnel (exchange) couplings and anisotropic g-tensors. This is the architecture used in the present device. Consequently, the Hamiltonian cannot be cast into Eq. (20) and an additional rotation of the spin has to be taken into account [8]. Fortunately, the ‘‘additional’’ rotation from the exchange interaction can be absorbed into the rotation caused by the differences in g-tensor for a fixed magnetic field setting. In this case the total two-qubit Hamiltonian is given by

$$H_{2\text{Q}} = H_{\text{Q1}} + H_{\text{Q2}} + H_{\text{coup,iso}} + H_{\text{coup,SOI}}, \quad (24)$$

where the first three terms are given in Eqs. (22)-(23). The last term is caused by the spin-orbit interaction and is given by

$$H_{\text{coup,SOI}} = P_{2\text{Q}} U_{ij,kl} \left[\left(\frac{\mathbf{S}_i \cdot \mathbf{J}_{ik} \mathbf{S}_k}{\hbar^2} - \frac{1}{4} \right) + \left(\frac{\mathbf{S}_j \cdot \mathbf{J}_{jl} \mathbf{S}_l}{\hbar^2} - \frac{1}{4} \right) \right] U_{ij,kl}^\dagger P_{2\text{Q}} - H_{\text{coup,iso}}, \quad (25)$$

$$= \frac{1}{2} \begin{bmatrix} 0 & 0 & 0 & J_{\perp 2,ij,kl}^{\text{SO}} \\ 0 & 0 & J_{\perp 1,ij,kl}^{\text{SO}} & J_{a 2,ij,kl}^{\text{SO}} \\ 0 & J_{\perp 1,ij,kl}^{\text{SO},*} & 0 & J_{a 1,kl,ij}^{\text{SO}} \\ J_{\perp 2,ij,kl}^{\text{SO},*} & J_{a 2,ij,kl}^{\text{SO},*} & J_{a 1,kl,jk}^{\text{SO},*} & -J_{\parallel,ij,kl}^{\text{SO}} \end{bmatrix}, \quad (26)$$

where P_{2Q} is the projector on the two-qubit subspace,

$$U_{ij,kl} = U_{\phi_{ij}} U_{\phi_{kl}} e^{i\mathbf{v}_{ij} \cdot \mathbf{S}_{ij}^0 / \hbar} e^{i\mathbf{v}_{kl} \cdot \mathbf{S}_{kl}^0 / \hbar}, \quad (27)$$

is the combination of the single S - T qubit basis transformation from the previous section, and $\mathcal{J}_{ik(jl)}$ is the exchange tensor between the spins in quantum dot pair ik (jl) in the spin-orbit basis [8] of quantum dot pair ij and kl . We also note that the full characterization of all elements cannot be resolved with our current operation regime and measurement setup, as high-fidelity sequential spin readout is required. For example, the $J_{\perp 2,ij,kl}^{\text{SO}}$ term could be characterized in the regime where the energies of the $|SS\rangle$ and $|T_-T_-\rangle$ states are identical but energetically separated from the other states. Therefore, we consider for simplicity an isotropic model to describe the swapping dynamics which fits well to the observations.

Simulation of the two-qubit energy spectrum To compute the two-qubit energy spectrum between Q3 and Q4 in the main text (Fig. 3b), we use the Hamiltonian of (21) and Eq. (7) and the estimated single-qubit parameters at $B = 10$ mT. Explicitly, we use $U_{Q3} = 290$ GHz, $U_{Q4} = 326$ GHz, $t_{Q3} = 3$ GHz, $t_{Q4} = 2.8$ GHz, $\varepsilon_{Q3} = -174$ GHz, $\bar{g}_{Q3} = 0.37$, $\bar{g}_{Q4} = 0.35$, and assume for simplicity a homogeneous $\Delta_{\text{SO},ij} = \Delta_{\text{SO},kl} = 10$ MHz. For the two-qubit interaction between Q3 and Q4, we use $H_{\text{coup,iso}}$ with $J_{\text{coup}} = (J_{ik} + J_{jl})/2$. We have estimated the inter-qubit exchange using $t_{ik} = 2$ GHz and $t_{jl} = 0.4$ GHz and $\varepsilon_{ik} = (\varepsilon_{ij} - \varepsilon_{kl} + \mu_0)/2$ and $\varepsilon_{jl} = (\varepsilon_{kl} - \varepsilon_{ij} + \mu_0)/2$ by assuming the difference between the chemical potential offsets of two qubits $\mu_0 = \mu_{ij} - \mu_{kl} = 0$.

Simulation of the state transfer For the simulation of the state transfer in the main text (Fig. 4b), we use the Hamiltonian of Eq. (23) for the SWAP operations with $J_{\text{coup}} = 95$ MHz and a single-qubit x -axis rotation frequency of Q4 of 13 MHz.

-
- [1] Hendrickx, N. *et al.* A single-hole spin qubit. *Nat. Commun.* **11**, 3478 (2020).
 - [2] van Diepen, C. J. *et al.* Quantum simulation of antiferromagnetic Heisenberg chain with gate-defined quantum dots. *Phys. Rev. X* **11**, 041025 (2021).
 - [3] Jirovec, D. *et al.* Dynamics of hole singlet-triplet qubits with large g -factor differences. *Phys. Rev. Lett.* **128**, 126803 (2022).
 - [4] Shulman, M. D. *et al.* Demonstration of entanglement of electrostatically coupled singlet-triplet qubits. *Science* **336**, 202–205 (2012).
 - [5] Wang, C.-A. *et al.* Probing resonating valence bonds on a programmable germanium quantum simulator. *npj Quantum Inf.* **9**, 58 (2023).
 - [6] Burkard, G., Ladd, T. D., Pan, A., Nichol, J. M. & Petta, J. R. Semiconductor spin qubits. *Rev. Mod. Phys.* **95**, 025003 (2023).
 - [7] Danon, J. & Nazarov, Y. V. Pauli spin blockade in the presence of strong spin-orbit coupling. *Phys. Rev. B* **80**, 041301 (2009).
 - [8] Geyer, S. *et al.* Two-qubit logic with anisotropic exchange in a fin field-effect transistor. *arXiv preprint arXiv:2212.02308* (2022).
 - [9] Burkard, G., Loss, D. & DiVincenzo, D. P. Coupled quantum dots as quantum gates. *Phys. Rev. B* **59**, 2070–2078 (1999).
 - [10] Jirovec, D. *et al.* A singlet-triplet hole spin qubit in planar ge. *Nat. Mater.* **20**, 1106–1112 (2021).
 - [11] Bravyi, S., Divincenzo, D. P. & Loss, D. Schrieffer-Wolff transformation for quantum many-body systems. *Annals of Physics* **326**, 2793 (2011).
 - [12] Chirolli, L. & Burkard, G. Decoherence in solid-state qubits. *Advances in Physics* **57**, 225–285 (2008).
 - [13] Lawrie, W. I. L. *et al.* Simultaneous single-qubit driving of semiconductor spin qubits at the fault-tolerant threshold. *Nature Communications* **14**, 3617 (2023).
 - [14] Hendrickx, N. W. *et al.* Sweet-spot operation of a germanium hole spin qubit with highly anisotropic noise sensitivity. *arXiv:2305.13150* (2023).